

# An infrared survey of brightest cluster galaxies: Paper I

Alice C. Quillen, Nicholas Zufelt, Jaehong Park

*Department of Physics and Astronomy, University of Rochester, Rochester, NY 14627*

`aquillen@pas.rochester.edu`, `zufelt72@potdham.edu`, `jaehong@pas.rochester.edu`

Christopher P. O'Dea, Stefi A. Baum, George Privon, Jacob Noel-Storr

*Department of Physics, Rochester Institute of Technology, 84 Lomb Memorial Drive,  
Rochester, NY 14623-5603*

`odea@cis.rit.edu`, `baum@cis.rit.edu`, `gcp1035@cis.rit.edu`, `jake@cis.rit.edu`

Alastair Edge

*Institute for Computational Cosmology, Department of Physics, Durham University,  
Durham DH1 3LE*

`alastair.edge@durham.ac.uk`

Helen Russell, Andy Fabian

*Institute of Astronomy, Madingley Rd., Cambridge, CB30HA, UK*

`hrr27@ast.cam.ac.uk`

Megan Donahue

*Michigan State University, Physics and Astronomy Dept., East Lansing, MI 48824-2320*

`donahue@pa.msu.edu`

Joel N. Bregman

*University of Michigan, Physics Dept., Ann Arbor, MI 48109*

`jbregman@umich.edu`

Brian R. McNamara

*Department of Physics & Astronomy, University of Waterloo, 200 University Avenue  
West, Waterloo, Ontario, Canada N2L 3G1*

`mcnamara@uwaterloo.ca`

&

Craig L. Sarazin

*Department of Astronomy, University of Virginia, P.O. Box 400325, Charlottesville, VA  
22904-4325*

sarazin@virginia.edu

## ABSTRACT

We report on an imaging survey with the *Spitzer Space Telescope* of 62 brightest cluster galaxies with optical line emission. These galaxies are located in the cores of X-ray luminous clusters selected from the ROSAT All-Sky Survey. We find that about half of these sources have a sign of excess infrared emission; 22 objects out of 62 are detected at 70  $\mu\text{m}$ , 18 have 8 to 5.8  $\mu\text{m}$  flux ratios above 1.0 and 28 have 24 to 8  $\mu\text{m}$  flux ratios above 1.0. Altogether 35 of 62 objects in our survey exhibit at least one of these signs of infrared excess. Four galaxies with infrared excesses have a 4.5/3.6  $\mu\text{m}$  flux ratio indicating the presence of hot dust, and/or an unresolved nucleus at 8  $\mu\text{m}$ . Three of these have high measured  $[\text{OIII}](5007\text{\AA})/\text{H}\beta$  flux ratios suggesting that these four, Abell 1068, Abell 2146, and Zwicky 2089, and R0821+07, host dusty active galactic nuclei (AGNs). 9 objects (including the four hosting dusty AGNs) have infrared luminosities greater than  $10^{11} L_{\odot}$  and so can be classified as luminous infrared galaxies (LIRGs). Excluding the four systems hosting dusty AGNs, the excess mid-infrared emission in the remaining brightest cluster galaxies is likely related to star formation.

*Subject headings:* stars: formation – galaxies: clusters: general – galaxies: active – galaxies: elliptical and lenticular, cD – cooling flows – infrared: galaxies

## 1. Introduction

X-ray observations of many galaxy clusters show a density increase and a temperature decrease toward the centers of these systems, implying that gas should be cooling at rates of a few to  $1000 M_{\odot} \text{ yr}^{-1}$  (e.g., Allen 2000). A number of studies have found evidence for cooled gas and star formation in galaxy clusters, but at a rate below that corresponding to the cooling rate predicted from the X-ray observations (e.g., McNamara & O’Connell

1989; Cardiel et al. 1998; Crawford et al. 1999; Bregman et al. 2006). Although mechanisms to counteract radiative cooling of the intracluster medium have been identified (e.g., Birzan et al. 2004; Rafferty et al. 2006; Dunn & Fabian 2006; Peterson & Fabian 2006; McNamara & Nulsen 2007), these energy sources do not seem to be sufficiently efficient to shut off cooling altogether. Up to  $10^{11} M_{\odot}$  molecular gas is detected in BCGs with the largest mass deposition rates (e.g., Edge et al. 2002; Salomé & Combes 2003). Most cooling flow systems exhibit optical emission-lines such as  $H\alpha$  (Heckman 1981; Hu, Cowie & Wang 1985). Emission line spectroscopy suggests that some of the emission is due to photoionization and heating by hot stars (Voit & Donahue 1997). The gulf between the spectral limits on the condensation rates and the sink of cooling material, the primary objection to cooling flows, has narrowed dramatically. In some systems, star formation rates are close to the X-ray and far UV estimates of the rates of gas condensation (Hicks & Mushotzky 2005; Rafferty et al. 2006; McNamara 2004).

To probe the efficiency of cooling and star formation in cluster galaxies, we aim to provide more direct measurements of the star formation rate in central cluster galaxies using broad band images obtained with the *Spitzer Space Telescope* (SST). Recent work using SST observations of a few brightest cluster galaxies (BCGs) includes the study by Egami et al. (2006) finding that the majority of BCGs are not infrared luminous. This study of 11 galaxies suggested that star formation was responsible for non-AGN excess infrared emission in 3 BCGs and that star formation was taking place primarily in objects with high X-ray luminosity. Two of the objects studied by Egami et al. (2006) have estimated infrared luminosities classifying them as Luminous Infrared Galaxies (LIRGs),  $10^{11} < L_{\text{IR}} < 10^{12} L_{\odot}$ . Star formation rates for the infrared luminous objects were approximately 10 times lower than the mass deposition rates. While the galaxies studied by Egami et al. (2006) are moderately distant ( $0.15 < z < 0.5$ ), Donahue et al. (2007) found that the BCG in the nearby ( $z = 0.0852$ ) cluster Abell 2597 can also be classified as a LIRG.

In this paper we build on the previous studies of a small number of BCGs (Egami et al. 2006; Donahue et al. 2007) with an imaging survey of 62 BCGs using the *Spitzer Space Telescope* (SST). In this paper we describe the sample and survey data and briefly discuss the morphology seen in the images. Using aperture photometry we assemble spectral energy distributions (SEDs) of the central regions of the galaxies and identify the sources that have infrared excesses and estimate their infrared luminosities. Using infrared colors and morphology (whether a central source was red and unresolved) and optical emission line ratios we differentiate between sources with infrared emission consistent with contribution from a dusty AGN and those likely dominated by star formation. Comparison data are assembled to search for correlations between infrared luminosities and other cluster properties; however, the actual comparisons are done in a companion paper (paper II; O’Dea et al. 2007). In

this paper all luminosities have been corrected or computed to be consistent with a Hubble constant  $H_0 = 70 \text{ Mpc}^{-1} \text{ km s}^{-1}$  and a concordant cosmology ( $\Omega_M = 0.3$  and flat).

## 2. Images

### 2.1. Sample

The sample was chosen to investigate the impact of optical emission lines, known to be a good indicator of a cool core cluster (Edge et al. 1992; Peres et al. 1998), on the mid-infrared emission of BCGs in a representative sample of clusters. The sample was principally selected from the comprehensive optical spectral survey of BCGs in 215 ROSAT-selected clusters of Crawford et al. (1999). The Crawford et al. study includes 177 clusters (or 87%) from the Brightest Cluster Sample (BCS, Ebeling et al. 1998), 17 (17%) from the extended Brightest Cluster Sample (BCS, Ebeling et al. 2000), 11 (2%) of the ROSAT-ESO Flux Limited X-ray (REFLEX) cluster sample (Böhringer et al. 2004) and 10 clusters below the flux limit from these 3 samples ( $< 3 \times 10^{-12} \text{ erg cm}^{-2} \text{ s}^{-1}$  0.1-2.4 keV) or at low galactic latitude ( $|b| < 20^\circ$ ). Optical emission lines are detected in 27% of the Crawford et al. sample and we select all BCGs detected brighter than  $0.5 \times 10^{-15} \text{ erg cm}^{-2} \text{ s}^{-1}$  extracted from a  $1.3''$  slit in either  $\text{H}\alpha$  or  $[\text{NII}]$  from the BCS, eBCS and REFLEX samples. This flux selection is a factor of a few above the detection limit of this study so allows for any variation in depth due to observing conditions and continuum strength. Excluding three objects where the lines were affected by either atmospheric absorption (A671), high declination (A2294) or a badly placed cosmic ray (RXJ1750.2+3505), this gives a total of sample of 64 BCGs. To this sample we add the 6 BCS BCGs that are known to exhibit line emission but were not observed by Crawford et al. to ensure that we have complete sampling of the BCS line emitters. Of this sample of 70, 16 have existing GTO or GO Spitzer observations, e.g. M87/3C274, NGC 383/3C31 and NGC7237/3C442A in the study of powerful FRI radio galaxies by Birkinshaw and A1835, Zw3146 and Zw7160 in the sample by Egami et al. (2006), leaving 54 to be observed with imaging by the SST.

For completeness and to include clusters in both hemispheres, we have supplemented the remaining total of 54 line emitting BCGs from the study by Crawford et al. with four well-studied BCGs from the Edge et al. (1990) all-sky sample (A85, A3112, A4059 and PKS0745-191), Abell S1101 (frequently referred to as Sersic159-01) from REFLEX and Z348 from the eBCS which shows very strong emission lines in its spectrum in the SDSS. One BCG from a cluster just below our nominal X-ray flux limit was included, A11, as it is the only remaining CO detection by Edge (2001) and Salomé & Combes (2003) not covered by our selection for a Spitzer observation. This selection gives a sample of 61 line emitting BCGs

to which through an oversight in the compilation we added one non-line emitting BCG from Crawford et al., A2622, to give the total of 62 observed in this program and listed in Table 1. The redshift distribution of the sample is shown in Figure 1. At a redshift of  $z = 0.1$ , near the median of the sample, 1 arcsec corresponds to a distance of 1.84 kpc.

We believe the BCGs selected for this study provide a direct test of the link between optical line emission and MIR emission for individual objects but also for a statistically significant and complete X-ray selected BCS sample.

The 62 BCGs of our total observed sample are listed in Table 1 and the redshift distribution is shown in Figure 1. At a redshift of  $z=0.1$ , near the median for the sample, 1 arcsec corresponds to a distance of 1.84 kpc.

## 2.2. IRAC data

The 3.6, 4.5, 5.8 and 8.0  $\mu\text{m}$  broad band images were obtained during Cycle 3 (2007-2008) using the Infrared Array Camera (IRAC; Fazio et al. 2004) on board the *Spitzer Space Telescope*. One frame per band was observed with a 12 second frame times a 9 position random medium step dither pattern resulting in 108 seconds total on source integration time. Each image has a field of view of  $5'2 \times 5'2$ . Post basic calibrated data were used to make color maps and generate photometric measurements.

Following the previous work by Egami et al. (2006), we have begun our study by measuring fluxes in an aperture of diameter  $12''2$ . Sky annulus radii and aperture corrections are listed in the notes to Table 2. The aperture photometry (as described here) is sufficiently accurate to separate between AGNs and star forming objects and estimate infrared luminosities, allowing a survey of the energetics of our sample of BCGs. We note that spectral energy distributions created from our aperture photometry are not accurate enough to allow stellar population models to be compared in detail. Moreover, since our sample spans a range in distance and the IRAC images exhibit color gradients, model spectral energy distributions should in future be fit to measurements from different regions in each galaxy. We plan this in future investigations.

## 2.3. MIPS data

The 24.4 and 70  $\mu\text{m}$  images were obtained using the Multiple Imaging Photometer for Spitzer (MIPS; Rieke et al. 2004). The exposure times at 24  $\mu\text{m}$  and 70  $\mu\text{m}$  were 3 cycles of 10 seconds each. Basic calibrated data were reduced with the MOPEX (Makovoz & Khan 2005)

software which performs interpolation and co-addition of FITS images. The final 24 and 70  $\mu\text{m}$  images have a field of view of  $7'.5 \times 8'.2$  and  $3' \times 8'$ , respectively. To make photometric measurements we have used the same aperture radii and corrections as Egami et al. (2006); these are listed in the notes to Table 2.

## 2.4. Comparison data

Comparison data in other spectral bands for the BCGs in our sample are listed in Table 1. Brightest cluster galaxies could host star formation, an active galactic nucleus, as well as a cooling flow. When available, Table 1 lists X-ray, radio (1.4 GHz) and  $\text{H}\alpha$  luminosities and  $[\text{OIII}](5007)/\text{H}\beta$  flux ratios. X-ray luminosities provide a constraint on the mass in and radiative losses from the hot ICM. The  $\text{H}\alpha$  recombination line is excited by emission from newly formed hot stars or from an AGN. To discriminate between the presence of an AGN and star formation we have sought a measure of the radiation field in the  $[\text{OIII}](5007\text{\AA})/\text{H}\beta$  optical line ratio and an estimate of the radio luminosity.

X-ray luminosities in almost all cases, are based on 0.1-2.4 keV ROSAT fluxes.  $\text{H}\alpha$  luminosities are based on measurements by Crawford et al. (1999), or in a few cases drawn or estimated from the literature (see citations given in the notes for Table 1). The  $[\text{OIII}](5007)$  to  $\text{H}\beta$  flux ratios were taken from measurements in Table 6 by Crawford et al. (1999) and from spectroscopic line measurements listed in the Sloan Digital Sky Survey (SDSS) archive. Comparison VLA 1.4 GHz radio fluxes were drawn from the Faint Images of the Radio Sky at Twenty cm (FIRST) survey (Becker et al. 1995; White et al. 1997) and the NRAO VLA Sky Survey (NVSS) (Condon et al. 1998). These have spatial resolutions of  $5''$  (B configuration) and  $45''$  (D configuration), and noise levels of  $\sim 140$  and  $450 \mu\text{Jy}$ , respectively. Luminosities at 1.4 GHz were computed using integrated flux densities<sup>1</sup>. For a few objects, multiple sources were within a few arcseconds of the BCG galaxy position. In these cases we looked at the images. When objects appeared to be radio doubles we used the NVSS integrated flux (see notes listed in Table 1).

---

<sup>1</sup>NVSS: <http://www.cv.nrao.edu/nvss/NVSSlist.shtml>  
 FIRST: <http://sundog.stsci.edu/cgi-bin/searchfirst>

### 3. Results

We discuss the morphology of the objects and the spectral energy distributions which show that about 1/3 of the BCGs exhibit some form of IR excess.

#### 3.1. Morphology

In Figure 2 we show small ( $2' \times 2'$ ) gray scale images of all the galaxies in our sample. A number of them show bright sources at 24 and 70  $\mu\text{m}$ . All but one of the sources (Z9077) was detected at 24  $\mu\text{m}$ , but only about 1/4 of the sample were detected at 70  $\mu\text{m}$ . Also shown in Figure 2 are color maps made from sky subtracted 8.0 and 3.6  $\mu\text{m}$  IRAC images. Abell 1068, Abell 2146, R0821+08 and Zw 2089 have prominent unresolved red central sources. NGC 4104 and Abell 11 have faint red and unresolved red nuclei. The remaining BCGs have resolved weak (e.g., Abell 1664) or no color gradients evident in the color maps.

Two of the objects in our survey (R0751+50 and Abell 2627) are binary; each has two potential BCGs. For R0751+50 the eastern galaxy contains a nucleus that is quite bright at 24  $\mu\text{m}$  but has no strong color gradient in the 3.6 to 8.0  $\mu\text{m}$  ratio color map, and so is probably forming stars. For Abell 2627 the northern galaxy is bright at 24  $\mu\text{m}$  and is also likely to be forming stars.

The galaxy cluster with the most interesting morphology is R0751+50 which contains a bright oval or elliptical ring at seen most prominently at 8  $\mu\text{m}$  surrounding the two elliptical binary galaxies. The ring may be a large spiral arm, is seen primarily at 8  $\mu\text{m}$  but is also faintly seen at 24  $\mu\text{m}$ . At a redshift of 0.0236 the ring has a radius from the midpoint between the two ellipticals of  $30'' \sim 14$  kpc. A faint counterpart is seen in Galaxy Evolution Explorer (*GALEX*) images suggesting that the ring is also emitting in the UV. The bright 8  $\mu\text{m}$  emission in the ring may be due to a dust emission feature at 7.7  $\mu\text{m}$ .

#### 3.2. Spectral energy distributions

In Figure 3 we show spectral energy distributions for all of the BCGs using aperture photometry listed in Table 2. To minimize the contribution from the galaxy stellar component we have used apertures for the IRAC measurements that are smaller than those for the MIPS photometric measurements. Small apertures cannot be used for long wavelength photometric measurements because of the larger diffraction pattern; however, the mid-infrared excess and longer wavelength emission are unresolved in these larger apertures.

Thus the spectral energy distributions give us an estimate for the contribution at all plotted wavelengths within the IRAC apertures.

We have classified the spectral energy distributions into 4 different types depending on the flux ratio  $F_{8.0\mu\text{m}}/F_{5.8\mu\text{m}}$ . We chose this flux ratio as it increases when there is emission from the PAH feature at  $7.7\ \mu\text{m}$  prominent in star forming galaxies. This flux ratio is also more robustly measured compared to the  $F_{24\mu\text{m}}/F_{8\mu\text{m}}$  color ratio which contains much more scatter, although the two colors are correlated in our sample. The correlation can be seen clearly in the slopes of the spectral energy distributions; sources that have red 8.0 to  $5.8\ \mu\text{m}$  flux ratios tend to have red 24 to  $8\ \mu\text{m}$  flux ratios. This correlation can also be seen in Figure 4 from the  $5.8/3.6\ \mu\text{m}$  and  $24/8\ \mu\text{m}$  colors.

In Figures 3a,b we show the 13 sources that have the reddest color ratios;  $F_{8\mu\text{m}}/F_{5.8\mu\text{m}} > 1.3$ . These sources have clear mid-infrared excesses (compared to a quiescent elliptical galaxy stellar population), and are bright at  $24\ \mu\text{m}$  and  $70\ \mu\text{m}$ . All of this color group were detected in both MIPS bands. They are separated into two figures to highlight those three with extreme red color (in Figure 3a) throughout all bands and those with red colors primarily in the  $8.0/5.8\ \mu\text{m}$  flux ratio but not the  $4.5/3.6\ \mu\text{m}$  flux ratio (in Figure 3b). The objects shown in Figure 3b could have elevated emission at  $8\ \mu\text{m}$  due to a  $7.7\ \mu\text{m}$  PAH emission feature that is prominent in star forming galaxies but are lacking hot dust associated with an AGN at shorter wavelengths. The dust emission feature may account for the high  $8\ \mu\text{m}$  flux compared to that at 24 microns for R0338+09.

Sources with  $1.0 < F_{8\mu\text{m}}/F_{5.8\mu\text{m}} < 1.3$  and  $0.75 < F_{8\mu\text{m}}/F_{5.8\mu\text{m}} < 1.0$  are shown in Figure 3c, and Figure 3d,e, respectively. The division in color space is made so that not too many spectral energy distributions lie on the same plot. In Figures 3f,g,h we show sources with color  $F_{8\mu\text{m}}/F_{5.8\mu\text{m}} < 0.75$ . Most of the objects with  $F_{8\mu\text{m}}/F_{5.8\mu\text{m}} < 1.0$  were not detected at  $70\ \mu\text{m}$ . Those with detected emission at  $70\ \mu\text{m}$  are also likely to contain dust that is heated by star formation even if they don't exhibit red colors at wavelengths below 8 or 24 microns. We note that the  $70\ \mu\text{m}$  images contain spurious structure in the sky background making accurate photometry difficult. To list an object as detected at  $70\ \mu\text{m}$  we required a clear and statistically significant source to be located at the expected galaxy position. The objects with color  $F_{8\mu\text{m}}/F_{5.8\mu\text{m}} < 0.75$  and lacking a detection at  $70\ \mu\text{m}$  are consistent with a quiescent stellar population dominated by emission from old stars.

It is clear from Figures 3a-h that a significant number of the BCGs in our sample have infrared excesses. 22 objects of 62 are detected at  $70\ \mu\text{m}$ , 18 have  $8\ \mu\text{m}$  to  $5.8\ \mu\text{m}$  flux ratios above 1.0 and 28 objects have  $24\ \mu\text{m}$  to  $8\ \mu\text{m}$  flux ratios about 1.0. Taking these three criteria together 35 objects of 62 have some kind of excess. As discussed by O'Dea et al. (2007) the infrared excesses are likely due to star formation with the exception of the four



objects that we discuss below that may be dominated by a dusty AGN.

We can consider the fraction of objects with IR excess that did not display  $H\alpha$  emission. Only one object in our sample was reported lacking emission lines, Abell 2622 (Owen et al. 1995). We did not find any evidence of infrared excess from this galaxy. 7 objects BCGs in our sample exhibited emission in NII and not  $H\alpha$ , of these 4 exhibited some form of infrared excess (A2055, A2627, R0000+08, and Z4905) and 3 did not (A1767, A2033, A4059). The fraction with some form of infrared excesses is not significantly different than that of the total sample. Unfortunately we lack a comparison sample of X-ray bright BCGs that lack optical emission lines. Correlations between infrared excess and other properties are discussed further in paper II.

### 3.2.1. Four Luminous AGN

The reddest sources (those in Figure 3a) are an interesting group containing Abell 2146, Abell 1068, and Zwicky 2089. These objects have red colors in all IRAC band ratios suggesting that very hot dust (a temperatures greater than 1000 K), emitting even at 4.5 microns is present (e.g., as seen for Seyfert galaxies, Alonso-Herrero et al. 2003). The short wavelength spectral energy distributions for these 3 objects differ from that of a quiescent population and from that of the objects with infrared excesses studied by Egami et al. (2006). Abell 2146, Abell 1068 and Zwicky 2089 have  $[OIII](5007)/H\beta$  ratios of 7.1, 3.7, and 6.2 respectively, consistent with the presence of a hard radiation source or AGN. The only other object in our sample with a high  $[OIII]/H\beta$  flux ratio in the Crawford et al. 1999 spectral study is Zw 3179 with  $[OIII]/H\beta = 4.8^{+2.2}_{-2.2}$  but both lines are weak so this ratio is uncertain. Therefore, there appears to be a strong correspondence between the optical line ratios and the presence of hot dust emission in the IRAC bands.

Compared to the other objects with red mid-infrared colors,  $F_{8\mu m}/F_{5.8\mu m} > 1.3$ , Abell 2146 has a blue color in the ratio  $F_{70\mu m}/F_{24\mu m}$ . Abell 2146 has a ratio of  $\sim 3.7$  compared to  $F_{70\mu m}/F_{24\mu m} \sim 7$  for Zw 2089 and 12 for Abell 1068. Abell 2146 could have a warmer dust temperature than the other objects with mid-infrared excesses suggesting that it is AGN dominated (Sanders et al. 1988; Armus et al. 2007). This BCG could have a spectral energy distribution similar to that of a Seyfert galaxy or a quasar. Abell 2146 has previously been classified as an AGN (Allen 1995), whereas previous studies found that Abell 1068 hosts an extended starburst (Allen 1995; McNamara et al. 2004).

Four BCGs have prominent red unresolved nuclear sources as seen from the 8.0/3.6 $\mu m$  color maps: Abell 1068, Abell 2146, Zw 2089 and R0821+07. The first three have evidence

for hot dust. R0821+07 has a red color  $F_{8\mu\text{m}}/F_{5.8\mu\text{m}} > 1.3$  but no evidence for hot dust from its  $F_{4.5\mu\text{m}}/F_{3.6\mu\text{m}}$  ratio. It also has a high ratio  $[\text{OIII}]/\text{H}\beta \sim 2.5$  ratio, so it too could host a more obscured dusty AGN.

### 3.3. Estimated infrared luminosities

Following the procedure used by Egami et al. (2006) we use the 8 and  $24\mu\text{m}$  fluxes to estimate the infrared luminosity. Previous studies (e.g., Spinoglio et al. 1995; Elbaz et al. 2002) have found that bolometric luminosities estimated from the  $15\mu\text{m}$  flux are less sensitive to dust temperature than those estimated from fluxes at other wavelengths. We estimate the flux at  $15\mu\text{m}$  with a linear interpolation of the 8 and  $24\mu\text{m}$  fluxes. Then the  $15\mu\text{m}$  flux is converted to an infrared luminosity  $L_{\text{IR}}$  using equation 13 by Elbaz et al. (2002) giving a relation between  $15\mu\text{m}$  observations and total infrared luminosity that has been established from *Infrared Space Observatory* (ISO) observations of quiescent and active galaxies;

$$L_{\text{IR}} = 11.1^{+5.5}_{-3.7} \times (\nu L_{\nu}[15\mu\text{m}])^{0.998}. \quad (1)$$

where both  $L_{\text{IR}}$  and  $\nu L_{\nu}[15\mu\text{m}]$  are in erg/s. Infrared luminosities are listed in Table 3. For galaxies that have no evidence of an infrared excess and have not been detected at  $70\mu\text{m}$ , this procedure significantly overestimates the infrared luminosity. We have checked that this estimate is approximately consistent with the luminosity at  $70\mu\text{m}$  for the objects that are not red at wavelengths shorter than  $8\mu\text{m}$  but are detected at  $70\mu\text{m}$  (e.g., that are shown in Figure 3h). Consequently we have listed infrared luminosities only for objects that have evidence of an infrared excess. We list only objects with  $F_{8.0}/F_{5.8\mu\text{m}} > 1.0$ , or  $F_{24}/F_{8\mu\text{m}} > 1.0$ , or that were detected at  $70\mu\text{m}$ . We find that 9 of the BCGs can be classified as LIRGs with  $10^{11}L_{\odot} < L_{\text{IR}} < 10^{12}L_{\odot}$ . The 9 LIRGs include the 4 that host dusty AGN. These 4 have luminosities which put them in the Seyfert/QSO transition region for IR luminosity (e.g., Rush, Malkan & Spinoglio 1993; Schweitzer et al. 2006). Thus, these are Type 2 luminous AGN.

## 4. Summary

We have presented Spitzer IRAC and MIPS photometry of a sample of 62 BCGs selected on cluster X-ray flux and BCG  $\text{H}\alpha$  or  $[\text{NII}]$  flux to favor objects in cool cluster cores. We find that one half to one-third of the sample show an infrared excess above that expected for the old stellar population. These results confirm the previous results of Egami et al. (2006), based on a sample of 11 BCGs in X-ray luminous clusters, that some BCGs in cool core

clusters show an infrared excess due to star formation.

An interesting difference between our survey and previous studies (Egami et al. 2006; Donahue et al. 2007) is the discovery of a small number of objects that host dusty AGNs, thanks to our much larger sample. Three galaxies exhibit red  $4.5/3.6\mu\text{m}$  flux ratios and unresolved nuclei seen in IRAC color maps indicating the presence of hot dust. These three, Abell 1068, Abell 2146, and Zwicky 2089, have measured high  $[\text{OIII}](5007)/\text{H}\beta$  flux ratios suggesting that they host a dusty AGN. An additional BCG, R0821+07, has a red unresolved nucleus at  $8\mu\text{m}$  and a high  $[\text{OIII}](5007)/\text{H}\beta$  ratio suggesting that it too hosts a dusty AGN.

These four BCGs have infrared luminosities greater than  $10^{11}L_{\odot}$  and so can be classified as LIRGs. A comparison between their infrared luminosity and 1.4 GHz radio luminosity yields ratios of  $10^6 - 10^7$  suggesting that they can be considered radio quiet. The only similar previously known object is the more distant ( $z = 0.44$ ) and hyperluminous infrared galaxy IRAS 09104+4109 (Fabian & Crawford 1995), also a BCG in an X-ray luminous cluster.

In addition to the 4 hosting AGNs, there are 5 other BCGs with infrared luminosities greater than  $10^{11}L_{\odot}$  that can be classified as luminous infrared galaxies (LIRGs). Excluding the AGNs, the remaining brightest cluster galaxies with infrared excesses are likely bright in the mid-infrared because of star formation as discussed in our companion paper (O’Dea et al. 2007). In this work we have discussed the identifications and broad properties of this sample. Our companion paper (paper II; O’Dea et al. 2007) searches for correlations between star formation rates, radio,  $\text{H}\alpha$ , CO and X-ray luminosities and mass deposition rates estimated from the X-ray observations. Planned future work includes fitting model spectral energy distributions to the observations.

We thank Eiichi Egami for helpful correspondence. This work is based on observations made with the Spitzer Space Telescope, which is operated by the Jet Propulsion Laboratory, California Institute of Technology under a contract with NASA. Support for this work at University of Rochester and Rochester Institute of Technology was also provided by NASA through an award issued by JPL/Caltech and by NSF grants AST-0406823 & PHY-0552695.

## REFERENCES

- Allen, S. W. 1995, MNRAS, 276, 947  
 Allen, S. W. 2000, MNRAS, 315, 269

- Alonso-Herrero, A., Quillen, A. C., Rieke, G. H., Ivanov, V.D., & Efstathiou, A. 2003, *AJ*, 126, 81
- Armus, L., et al. 2007, *ApJ*, 656, 148
- Becker, R. H., White, R. L., & Helfand, D. J. 1995, *ApJ*, 450, 559
- Birzan, L., Rafferty, D. A., McNamara, B. R., Wise, M. W., & Nulsen, P. E. J. 2004, *ApJ*, 607, 800
- Böhringer, H., et al. 2004, *A&A*, 425, 367
- Bregman, J. N., Fabian, A. C., Miller, E. D., & Irwin, J. A. 2006, *ApJ*, 642, 746
- Brinkmann, W., Siebert, J., Reich, W., Fuerst, E., Reich, P., Voges, W., Truemper, J., & Wielebinski, R. 1995, *A&AS*, 109, 147
- Cardiel, N., Gorgas, J., & Aragon-Salamanca, A. 1998, *Ap&SS*, 263, 83
- Condon, J. J., et al. 1998, *AJ*, 115, 1693
- Crawford, C. S., Allen, S. W., Ebeling, H., Edge, A. C., & Fabian, A. C. 1999, *MNRAS*, 306, 857
- David, L.P., Forman, W., & Jones, C. 1999, *ApJ*, 519, 533
- Donahue, M., Baum, S., Cote, P., Ferrarese, L., Goudfrooij, P., Jordan, A., Macchetto, D., Malhotra, S., O’Dea, C. P., Pringle, J., Rhoads, J., Sparks, W., & Voit, G. M. 2007, *ApJ*, in press
- Dunn, R. J. H. & Fabian A. C. 2006, *MNRAS*, 373, 959
- Ebeling, H., Edge, A. C., Böhringer, H., Allen, S. W., Crawford, C. S., Fabian, A. C., Voges, W., & Huchra, J. P. 1998, *MNRAS*, 301, 881
- Ebeling, H., Edge, A. C., Allen, S. W., Crawford, C. S., Fabian, A. C., & Huchra, J. P. 2000, *MNRAS*, 318, 333
- Edge, A. C., Stewart, G. C., Fabian, A. C., & Arnaud, K. A. 1990, *MNRAS*, 245, 559
- Edge, A. C., Stewart, G. C., & Fabian, A. C. 1992, *MNRAS*, 258, 177
- Edge, A. C., Wilman, R. J., Johnstone, R. M., Crawford, C. S., Fabian, A. C., & Allen, S. W. 2002, *MNRAS*, 337, 49

- Edge, A. C. 2001, MNRAS, 328, 762
- Egami, E., et al. 2006, ApJ, 647, 922
- Elbaz, D., Cesarsky, C. J., Chantal, P., Aussel, H., Franceschini, A., Fadda, D., & Chary, R. 2002, A&A, 384, 848
- Fabian, A. C., & Crawford, C. S. 1995, MNRAS, 274, L63
- Fazio, G. G., et al. 2004, ApJS, 154, 10
- Hatch, N. A., Crawford, C. S., & Fabian, A. C. 2007, MNRAS, 380, 33
- Heckman, T. M. 1981, ApJ, 250, L59
- Hicks, A. K., & Mushotzky, R. 2005, ApJ, 635, L9
- Hu, E. M., Cowie, L. L., & Wang, Z. 1985, ApJS, 59, 447
- Jaffe, W., Bremer, M. N., & Baker, K. 2005, MNRAS, 360, 748
- Jones, D. H., et al. 2004, MNRAS 355, 747
- Jones, D. H., Saunders, W., Read, M. A., & Colless, M. 2005, PASA, 22, 277
- Katgert, P., Mazure, A., den Hartog, R., Adami, C., Biviano, A., & Perea, J. 1998, A&AS, 129, 399
- Makovoz, D., & Khan, I. 2005, in ASP Conf. Ser. 347, Astronomical Data Analysis Software and Systems XIV, ed. P. Shopbell, M. Britton, & R. Ebert (San Francisco: ASP), 81
- McNamara, B. R., Wise, M. W., & Murray, S. S. 2004, ApJ, 601, 173
- McNamara, B. R., & O’Connell, R. W. 1989, AJ, 98, 2018
- Star Formation in Cluster Cooling Flows, McNamara, B. R., Proceedings of The Riddle of Cooling Flows in Galaxies and Clusters of Galaxies, held in Charlottesville, VA, May 31 - June 4, 2003, Eds. T. Reiprich, J. Kempner, and N. Soker., page 177
- McNamara, B. R. & Nulsen, P. E. J. 2007, ARA&A, 45, 117
- O’Dea, C. P., et al. 2007, in preparation
- Owen, F. N., Ledlow, M. J., & Keel, W. C. 1995, AJ, 109, 140

- Peres, C. B., Fabian, A. C., Edge, A. C., Allen, S. W., Johnstone, R. M., & White, D. A. 1998, MNRAS, 298, 416
- Peterson, J. R., & Fabian, A. C. 2006, Phys Rep, 427, 1
- Rafferty, D. A., McNamara, B. R., Nulsen, P. E. J., & Wise, M. W. 2006, ApJ, 652, 216
- Rieke, G. H., et al. 2004, ApJS, 154, 25
- Rush, B., Malkan, M. A., & Spinoglio, L. 1993, ApJS, 89, 1
- Sanders, D. B., Soifer, B. T., Elias J. H., Neugebauer, G., & Matthews, K. 1988, ApJ, 328, L35
- Salomé, P., & Combes, F. 2003, A&A, 412, 657
- Schweitzer, M., et al., 2006, ApJ, 649, 79
- Spinoglio, L., Malkan, M. A., Rush, B., Carrasco, L., & Recillas-Cruz, E. 1995, ApJ, 453, 616
- Voit, G. M., & Donahue, M. 1997, ApJ, 482, 242
- White, R. L., Becker, R. H., Helfand, D. J., & Gregg, M. D. 1997, ApJ, 475, 479
- Wilman, R. J., Edge, A. C., & Swinbank, A. M. 2006, MNRAS, 371, 93

Table 1. The brightest cluster galaxy sample and comparison luminosities

Cluster	RA (2000)	DEC (2000)	z	$L_X$ ( $10^{44}$ erg s $^{-1}$ )	Ref.	$L_{H\alpha}$ ( $10^{40}$ erg s $^{-1}$ )	[OIII]/H $\beta$	Ref.	$L_{1.4\text{GHz}}$ ( $10^{31}$ erg s $^{-1}$ Hz $^{-1}$ )	Ref.
Abell 11	00 12 33.8	−16 28 06	0.1510	0.99	1	120	...	3	6.0	1
Abell 85	00 41 50.4	−09 18 14	0.0551	5.55	2	0.4	...	1	0.42	1
Abell 115	00 55 50.6	+26 24 39	0.1970	10.4	3	13.9	0.4	2	158	1
Abell 262	01 52 46.5	+36 09 08	0.0166	0.31	3	0.3	1.1	2	0.042	1
Abell 291	02 01 43.1	−02 11 47	0.1960	4.81	2	28.6	0.3	2	1.4	2
Abell 646	08 22 09.6	+47 05 54	0.1268	2.76	3	17.3	0.8	1	2.3	2
Abell 795	09 24 05.3	+14 10 22	0.1355	3.70	3	11.6	1.8	2	5.5	2
Abell 1068	10 40 44.4	+39 57 12	0.1386	5.00	3	143	3.7	1	0.46	2
Abell 1084	10 44 32.9	−07 04 08	0.1329	4.56	2	4.8	...	2	1.6	2
Abell 1204	11 13 20.3	+17 35 41	0.1706	4.96	3	6.7	1	2	0.21	2
Abell 1361	11 43 39.5	+46 21 22	0.1167	2.27	3	8.1	0.9	2	32	2
Abell 1664	13 03 42.5	−24 14 41	0.1276	2.60	2	67.2	0.5	2	1.6	1
Abell 1668	13 03 46.6	+19 16 18	0.0640	0.95	3	1.3	1.7	2	0.95	2
Abell 1767	13 36 08.1	+59 12 24	0.0715	1.51	3	...	...		0.023	2
Abell 1885	14 13 43.6	+43 39 45	0.0900	1.49	3	3.1	0.3	2	0.92	2
Abell 1930	14 32 37.9	+31 38 49	0.1316	2.66	3	1.4	...	2	0.38	2
Abell 1991	14 54 31.4	+18 38 34	0.0595	0.86	3	0.7	...	2	0.33	2
Abell 2009	15 00 19.6	+21 22 11	0.1532	6.09	3	7.3	0.7	2	5.3	1
Abell 2033	15 11 26.6	+06 20 58	0.0780	1.40	3	...	...		8.6	2
Abell 2052	15 16 44.6	+07 01 18	0.0351	1.39	3	1.6	4.2	2	16	1
Abell 2055	15 18 45.8	+06 13 57	0.1019	2.98	3	...	...		14	1
Abell 2072	15 25 48.7	+18 14 11	0.1270	2.02 <sup>a</sup>	3	3.1	0.7	2	0.19	2
Abell 2146	15 56 13.8	+66 20 55	0.2343	6.67	4	92.4	7.1	2	2.6	1
Abell 2204	16 32 46.9	+05 34 33	0.1514	14.1	3	119	0.7	2	3.7	2
Abell 2292	17 57 06.7	+53 51 38	0.1190	1.26	5	2.7	0.3	2	2.3	1
Abell 2495	22 50 19.6	+10 54 13	0.0808	1.97	3	1.5	...	2	0.25	1
Abell 2622	23 35 01.4	+27 22 22	0.0610	0.62	3	...	...		0.72	1
Abell 2626	23 36 30.7	+21 08 49	0.0552	1.07	3	0.53	...	2	0.41	1
Abell 2627	23 36 42.4	+23 55 06	0.1270	2.20	3	...	...		<0.062	2
Abell 2665	23 50 50.6	+06 09 00	0.0567	1.12	3	0.32	0.2	2	0.44	1
Abell 3112	03 17 57.7	−44 14 18	0.0761	4.31	2	...	...		...	...
Abell 4059	23 57 00.7	−34 45 32	0.0475	1.80	2	...	...		7.1	1
IC 1262	17 33 02.1	+43 45 35	0.0331	0.30	3	0.10	1.5	2	0.26	1
NGC 4104	12 06 38.8	+28 10 27	0.0281	0.11	3	0.33	...	2	0.004	2

Table 1—Continued

Cluster	RA (2000)	DEC (2000)	z	$L_X$ ( $10^{44}$ erg s $^{-1}$ )	Ref.	$L_{H\alpha}$ ( $10^{40}$ erg s $^{-1}$ )	[OIII]/H $\beta$	Ref.	$L_{1.4\text{GHz}}$ ( $10^{31}$ erg s $^{-1}$ Hz $^{-1}$ )	Ref.
NGC 4325	12 23 06.6	+10 37 17	0.0259	0.11	3	0.39	0.9	1	<0.001	2
NGC 5096	13 20 14.6	+33 08 39	0.0360	0.14	3	0.31	2	2	0.26	2
NGC 6338	17 15 22.6	+57 24 43	0.0282	0.24	3	0.66	0.8	2	0.09	2
PKS0745-191	07 47 31.35	-19 17 39.7	0.1028	16.4	6	70	...	3	66	1
RXC J0000.1+0816	00 00 07.1	+08 16 49	0.0400	0.22	3	...	...		0.32	1
RXC J0338.6+0958	03 38 40.5	+09 58 12	0.0338	2.20	3	9.6	0.6	2	0.17	1
RXC J0352.9+1941	03 52 58.9	+19 41 00	0.1090	2.50	3	33.8	0.6	2	0.57	1
RXC J0439.0+0520	04 39 02.2	+05 20 45	0.2080	6.28	3	70.6	1.2	2	10.7	2
RXC J0751.3+5012	07 51 19.9	+50 14 07	0.0236	0.13	3	0.87	...	1	...	...
RXC J0821.0+0751	08 21 02.4	+07 51 47	0.1100	1.29	4	17.7	2.5	2	0.066	2
RXC J1442.3+2218	14 42 19.4	+22 18 13	0.0970	1.63	3	2.7	1.7	2	0.47	2
RXC J1532.9+3021	15 32 53.8	+30 21 00	0.3615	23.3	3	427	0.6	1	22.9	1
RXC J1720.1+2637	17 20 10.1	+26 37 32	0.1611	10.6	3	25.4	0.2	1	6.5	1
RXC J2129.6+0005	21 29 39.9	+00 05 23	0.2346	13.9	3	28.5	0.2	1	4.1	2
S1101	23 13 58.8	-42 43 38	0.0564	1.84	2	9.98	...	4	...	...
Zw235	00 43 52.1	+24 24 22	0.0830	1.93	3	2.3	0.8	2	0.87	1
Zw348	01 06 49.3	+01 03 23	0.2535	7.37	4	195	0.6	1	0.71	2
Zw808	03 01 38.2	+01 55 15	0.1690	4.20	3	3.3	...	2	32.3	1
Zw1665	08 23 21.7	+04 22 22	0.0311	0.22	3	0.41	...	1	0.033	2
Zw2089	09 00 36.8	+20 53 43	0.2350	8.10	3	265	6.2		1.5	2
Zw2701	09 52 49.2	+51 53 06	0.2150	7.89	3	4.6	1.3	1	1.9	2
Zw3179	10 25 58.0	+12 41 09	0.1432	3.14	3	6.6	4.8	1	5.1	2
Zw3916	11 14 21.9	+58 23 20	0.2040	4.51	4	10.6	0.8	1	8.2	1
Zw4905	12 10 16.8	+05 23 11	0.0766	0.70	3	...	...		<0.006	2
Zw8193	17 17 19.1	+42 26 59	0.1754	8.04	4	95.6	0.8	2	11.8	2
Zw8197	17 18 11.8	+56 39 56	0.1140	1.85	3	8.5	1.0	1	1.2	2
Zw8276	17 44 14.5	+32 59 30	0.0750	2.34	3	9.7	0.8	2	1.3	1
Zw9077	23 50 35.4	+29 29 40	0.150	3.48	3	16.4	...	2	4.2	1

Note. — Columns 2 and 3 list the position of the brightest cluster galaxies. Most of these positions are those listed by Crawford et al. (1999). Column 4 lists redshifts. Column 5 lists X-ray luminosities based on 0.1-2.4 keV ROSAT fluxes, excepting for Abell 11 that is 0.5-2 keV. These have been corrected to be consistent with a Hubble constant  $H_0 = 70 \text{ Mpc}^{-1} \text{ km s}^{-1}$ . These luminosities have been taken from measurements listed in column 6. References – 1. David et al. (1999); 2. Böhringer et al. (2004); 3. Ebeling et al. (1998); 4. Ebeling et al. (2000); 5. Brinkmann et al. (1995); 6. Edge et al. (1990). Column 7 lists



luminosities in  $H\alpha$ . Column 8 lists  $[OIII](5007)/H\beta$  ratios. Optical line fluxes and ratios are derived from measurements described in column 9. References — 1. SDSS Spectral line measurements. 2. Tables 5 and 6 by Crawford et al. (1999). 3. Based on  $Pa\alpha$  fluxes measured by (Edge et al. 2002) 4. Table 1 by Jaffe et al. (2005). and an intrinsic  $H\alpha/Pa\alpha$  ratio of 8.46 for case B recombination at a temperature of  $10^4$  K and a density of  $100\text{ cm}^{-3}$ . Column 10 lists integrated luminosities per Hz at 1.4 GHz. The radio fluxes are taken from the surveys listed in column 11. The objects lacking luminosities were not at positions covered by either NVSS or FIRST surveys. References – 1. NVSS survey (Condon et al. 1998); 2. FIRST survey (Becker et al. 1995; White et al. 1997); Notes on individual radio observations: The following sources were extended and so the NVSS flux was used, not the FIRST flux: A85, A2052, A2055, R1720+26, and Z3916. The following had multiple components seen in the FIRST survey and these were added to estimate the total: A1361, A2033, and NGC5096. The following were extended in the NVSS images so fits images were used to integrate the total: A2009 and IC 1262, R0338+09, R1532+30. The non detections were given 3-sigma upper limits. Notes: <sup>a</sup>. The Rosat flux is contaminated by an AGN so the cluster X-ray luminosity is less than the number given here. Additional notes: We now describe objects lacking  $H\alpha$  luminosities in the table. 7 objects are classified as showing optical emission lines but lacking  $H\alpha$  emission. Objects with  $[NII]$  emission but no  $H\alpha$  reported by Crawford et al. (1999) are Abell 1767, Abell 2033, Abell 2055, Abell 2627, R0000+0816, and Z4905. Abell 4059 exhibits a similar spectrum with  $[NII]$  but no  $H\alpha$  as seen from the 6dFGS archive (Jones et al. 2004, 2006). A3112 exhibits  $[OII]$  emission (Katgert et al. 1998) but we have failed to find an report of its  $H\alpha$  emission. Through an over sight A2622 was included in the sample as it lacks emission lines (Owen et al. 1995).

Table 2. Infrared Photometry

Cluster	3.6 $\mu$ m (mJy)	4.5 $\mu$ m (mJy)	5.8 $\mu$ m (mJy)	8 $\mu$ m (mJy)	24 $\mu$ m (mJy)	70 $\mu$ m (mJy)
A0011	1.36	1.03	0.89	1.71	10.59	82
A0085	5.57	3.45	2.46	1.58	1.88	< 20
A0115	1.06	0.80	0.45	0.51	0.50	< 20
A0262	16.93	9.97	7.96	6.57	4.03	88
A0291	1.16	0.87	0.54	0.50	0.53	< 20
A0646	1.78	1.27	0.85	0.77	2.52	< 20
A0795	1.96	1.36	0.91	0.68	0.25	< 20
A1068	3.41	2.98	3.66	9.23	74.47	941
A1084	1.52	1.08	0.70	0.44	0.31	< 20
A1204	1.23	0.94	0.59	0.55	1.41	< 20
A1361	2.42	1.68	1.10	0.81	0.66	< 20
A1664	2.27	1.61	1.34	2.67	4.01	78
A1668	4.61	2.90	2.07	1.41	0.73	< 20
A1767	5.89	3.81	2.61	2.03	1.03	< 20
A1885	1.68	1.24	1.04	1.02	3.81	< 20
A1930	2.21	1.56	0.93	0.68	0.76	< 20
A1991	4.53	2.84	1.91	1.35	0.98	< 20
A2009	1.84	1.34	0.82	0.68	0.66	< 20
A2033	5.21	3.37	2.23	1.45	0.86	< 20
A2052	7.34	4.50	3.53	2.76	4.96	95
A2055	3.37	2.67	2.26	2.09	2.82	< 20
A2072	2.28	1.48	0.87	0.75	0.73	< 20
A2146	1.18	1.19	1.37	2.53	24.10	90
A2204	3.31	2.43	1.67	1.79	2.85	34
A2292	3.08	2.11	1.27	0.90	1.00	25
A2495	2.99	1.91	1.27	0.86	0.84	< 20
A2622	5.64	3.53	2.48	1.59	1.11	< 20
A2626	5.50	3.47	2.40	1.71	1.39	< 20
A2627	3.43	2.75	2.22	2.23	0.86	< 20
A2665	6.57	4.02	2.86	1.97	0.99	< 20

Table 2—Continued

Cluster	3.6 $\mu$ m (mJy)	4.5 $\mu$ m (mJy)	5.8 $\mu$ m (mJy)	8 $\mu$ m (mJy)	24 $\mu$ m (mJy)	70 $\mu$ m (mJy)
A3112	5.15	3.43	2.46	2.16	3.09	< 20
A4059	7.91	4.86	3.47	2.68	1.91	< 20
IC1262	7.59	4.54	3.27	2.26	1.21	< 20
NGC4104	17.51	10.60	9.45	12.38	27.90	540
NGC4325	10.04	5.96	4.46	3.41	2.36	< 20
NGC5096	7.15	4.33	3.09	2.02	1.32	< 20
NGC6338	17.77	10.45	7.73	5.11	3.16	30
PKS0745-191	3.95	2.76	2.12	2.87	10.34	154
R0000+08	6.95	4.20	3.07	2.22	2.42	53
R0338+09	9.43	5.70	4.55	9.61	2.39	78
R0352+19	2.04	1.57	1.41	2.07	5.14	132
R0439+05	1.71	1.36	0.85	0.92	2.10	55
R0751+50	13.14	7.80	5.87	3.94	2.58	44
R0751+50	13.62	8.09	6.02	3.78	1.81	< 20
R0821+07	2.52	1.81	1.62	7.03	18.00	327
R1442+22	2.83	1.89	1.26	0.97	0.63	< 20
R1532+30	0.82	0.71	0.48	0.95	3.77	112
R1720+26	2.11	1.55	0.93	0.81	0.48	< 20
R2129+00	1.45	1.16	0.74	0.56	1.04	< 20
S1101	4.90	3.05	2.15	1.60	1.27	< 20
Z0235	3.30	2.14	1.39	0.90	0.48	< 20
Z0348	0.63	0.58	0.43	1.13	4.54	44
Z0808	1.95	1.44	0.85	0.58	0.44	< 20
Z1665	8.20	4.88	3.63	2.31	1.59	< 20
Z2089	0.94	1.15	1.77	3.94	33.59	235
Z2701	1.21	0.92	0.57	0.37	0.36	< 20
Z3179	2.97	2.12	1.28	0.91	0.35	< 20
Z3916	1.43	1.12	0.62	0.49	0.41	< 20
Z4905	3.54	2.26	1.47	1.02	1.09	< 20
Z8193	4.92	3.73	2.40	3.99	10.66	177

Table 2—Continued

Cluster	3.6 $\mu$ m (mJy)	4.5 $\mu$ m (mJy)	5.8 $\mu$ m (mJy)	8 $\mu$ m (mJy)	24 $\mu$ m (mJy)	70 $\mu$ m (mJy)
Z8197	2.17	1.48	0.97	0.99	0.85	< 20
Z8276	3.24	2.15	1.63	1.62	3.22	22
Z9077	1.58	1.04	0.70	0.44	< 0.4	< 20

Note. — Aperture photometry at 3.6, 4.5, 5.8, 8 and 24.4  $\mu$ m were measured from the Band 1-4 IRAC images and Band 1 MIPS images. For the IRAC images we used an aperture diameter of 12'' and a sky annulus with inner and outer radii of 32'' and 48''. Aperture corrections taken from Table 5.7 of the IRAC data handbook were applied. These were 1.05, 1.05, 1.06, and 1.07 for Bands 1-4, respectively. At 24 $\mu$ m we used an aperture diameter of 26'' and a sky annulus with inner and outer radii of 20'' and 32'' as did Egami et al. (2006). Upper limits at 24 $\mu$ m and 70 $\mu$ m were estimated from the fluxes of the faintest sources in the field. At 70 $\mu$ m we used an aperture diameter of 35'' and a sky annulus with inner and outer radii of 39'' and 65'' as did Egami et al. (2006). The aperture correction for the 24 $\mu$ m and 70 $\mu$ m fluxes is 1.167 and 1.308, respectively based on Table 3.13 of the MIPS data handbook and is the same as that used by Egami et al. (2006). R0751+50 contains a pair of bright elliptical galaxies, hence two measurements are given, one for each galaxy. Abell 2627 is a galaxy pair; photometry is only given for the northern galaxy. R0338+09 has a nearby bright star which is adding to the uncertainty of the photometry.

Table 3. Estimated Infrared Luminosities of BCGs

Cluster	$L_{\text{IR}}$ ( $10^{44}\text{erg s}^{-1}$ )
Z2089*	64.68
A2146*	45.46
A1068*	44.61
R0821+07*	8.47
R1532+30*	22.62
Z8193*	13.70
Z0348*	11.92
A0011*	7.97
PKS0745-1	3.80
A1664	3.21
R0352+19	2.40
NGC4104	0.80
R0338+09	0.39
R0439+05*	4.17
A2204	3.23
A2627	1.59
A0115	1.30
Z8197	0.72
R2129+00	2.93
A1204	1.73
A0646	1.49
A2055	1.46
A0291	1.30
A1885	1.04
A3112	0.84
A2292	0.80
A1930	0.75
Z8276	0.74
Z4905	0.29
A0085	0.28

Table 3—Continued

Cluster	$L_{\text{IR}}$ ( $10^{44}\text{erg s}^{-1}$ )
A2052	0.24
R0000+08	0.20
NGC6338	0.18
R0751+50	0.10
A0262	0.08
A0795	<0.5
A1084	<4.1
A1361	<0.6
A1668	<0.3
A1767	<0.5
A1991	<0.3
A2009	<1.0
A2033	<0.4
A2072	<0.7
A2495	<0.3
A2622	<0.3
A2626	<0.3
A2665	<0.3
A4059	<0.3
IC1262	<0.1
NGC4325	<0.1
NGC5096	<0.1
R1442+22	<4.5
R1720+26	<1.1
S1101	<0.3
Z235	<0.3
Z808	<1.0
Z1665	<0.1
Z2701	<1.1
Z3179	<0.8

Table 3—Continued

Cluster	$L_{\text{IR}}$ ( $10^{44}\text{erg s}^{-1}$ )
Z3916	<1.3
Z9077	<0.6

Note. — Infrared luminosities are estimated from the flux at  $15\mu\text{m}$  as mentioned in Section 3.3 for BCGs that are either detected at  $70\mu\text{m}$ , have color ratio  $F_{8\mu\text{m}}/F_{5.8\mu\text{m}} > 1.0$  or  $F_{24\mu\text{m}}/F_{8.0\mu\text{m}} > 1.0$ . The top section contains four BCGs that are suspected to harbor dusty Type II AGNs. Z2089, A2146 and A1068 exhibit a red  $F_{4.5\mu\text{m}}/F_{3.6\mu\text{m}}$  color and all four have high  $[\text{OIII}](5007)/\text{H}\beta$  flux ratios. The second set is the remaining 10 BCGs with  $F_{8\mu\text{m}}/F_{5.8\mu\text{m}} > 1.3$ . The third section is the set of 6 clusters with  $1.0 < F_{8\mu\text{m}}/F_{5.8\mu\text{m}} < 1.3$ . The fourth set is the remaining BCGs with IR excesses. Specifically they have ratios  $F_{8\mu\text{m}}/F_{5.8\mu\text{m}} > 1.0$ ,  $F_{24\mu\text{m}}/F_{8.0\mu\text{m}} > 1.0$ , or a detected  $70\mu\text{m}$  flux. The BCGs marked with a \* can be classified as LIRGs since they have  $L_{\text{IR}}$  greater than  $10^{11}L_{\odot}$ . The last section contains upper limits for the remaining objects.

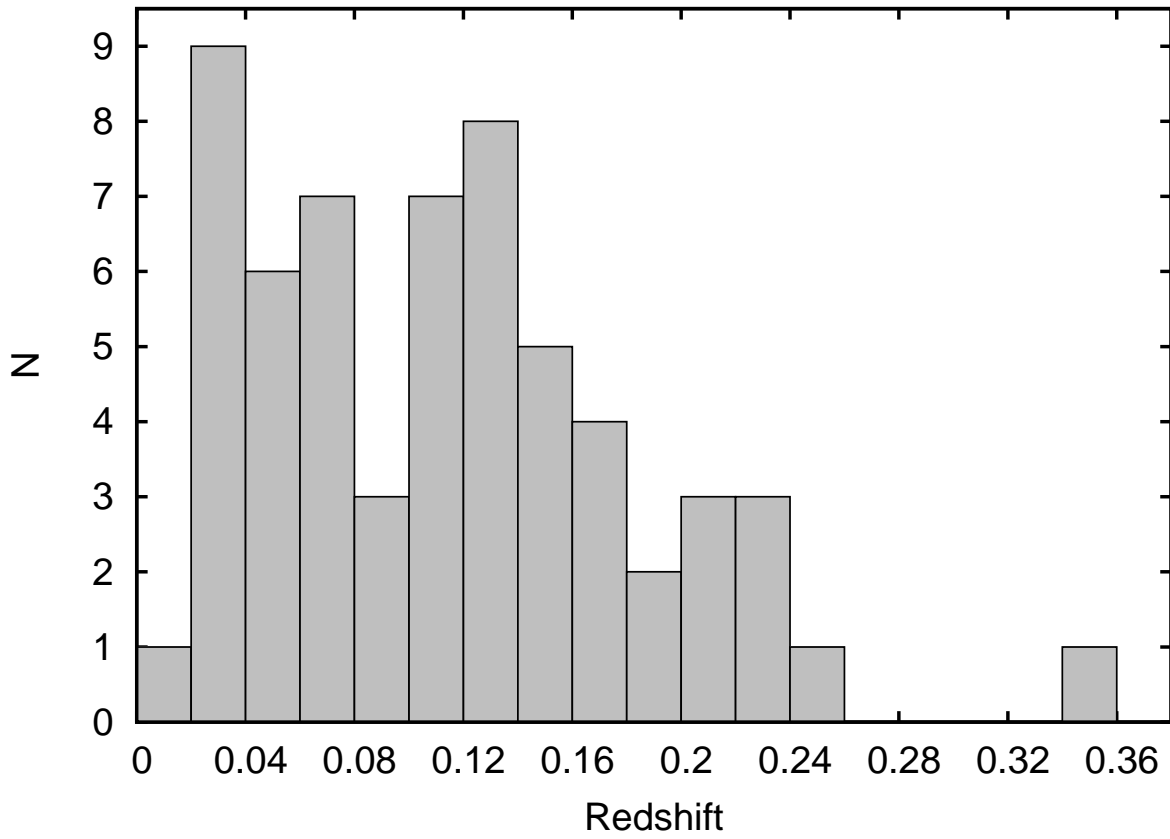


Fig. 1.— Redshift histogram giving the number of clusters in our sample in redshift bins.



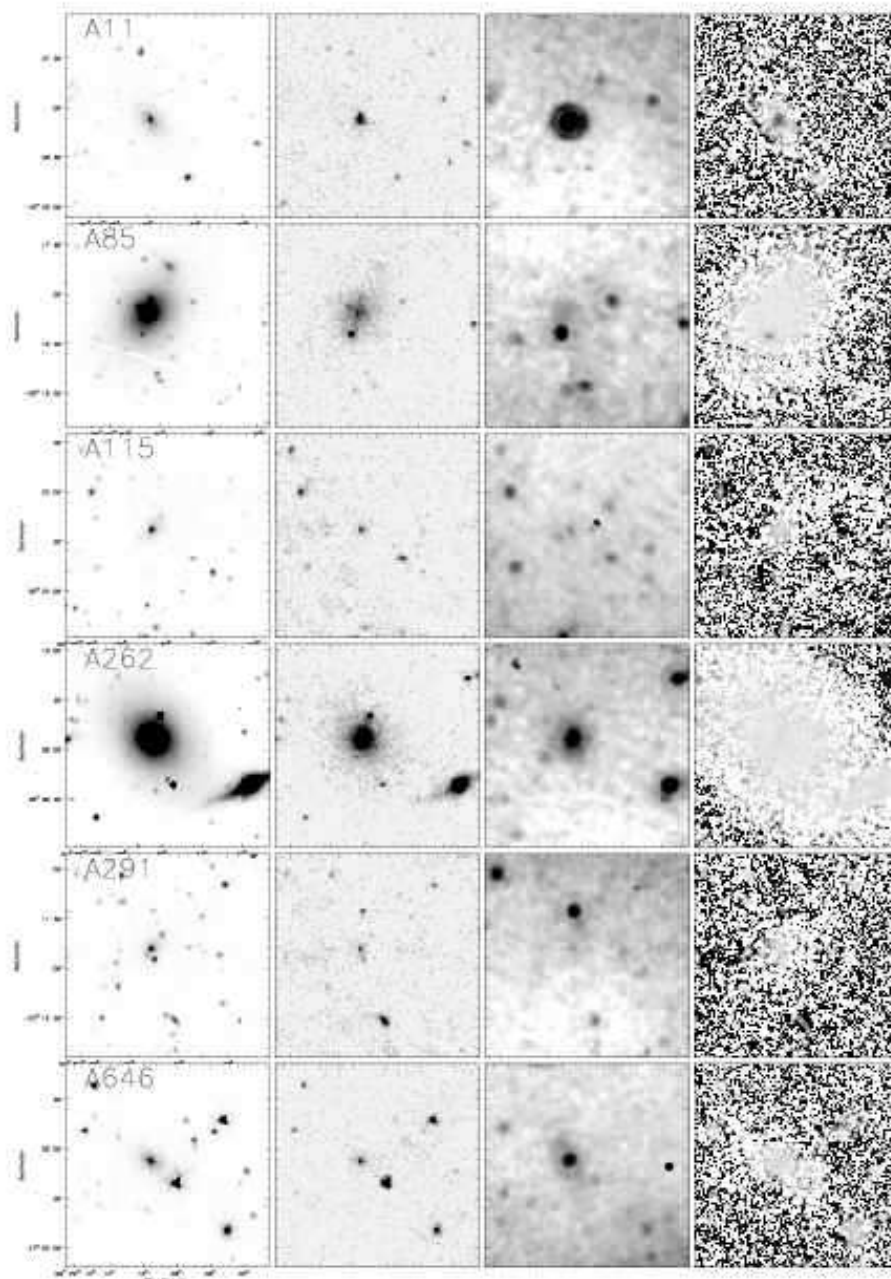


Fig. 2.— Each row shows one brightest cluster galaxy. From left to right are shown the IRAC Band 1 ( $3.6\ \mu\text{m}$ ), the IRAC Band 4 ( $8\ \mu\text{m}$ ) and the MIPS Band 1 ( $24\ \mu\text{m}$ ) images. The rightmost image shows a color map made from dividing sky subtracted IRAC Band 1 and 4 images in the same region. The region shown is  $2' \times 2'$ , and approximately centered on the brightest cluster galaxy. The color map is on a linear not log grayscale. Images that contain strong point sources at  $24\ \mu\text{m}$  sometimes exhibit diffraction rings and spikes (e.g., A1068 and A1664). Linear features in the images of PKS0745-19, R0338+09 and Z8193 are due to spikes caused by bright nearby stars.

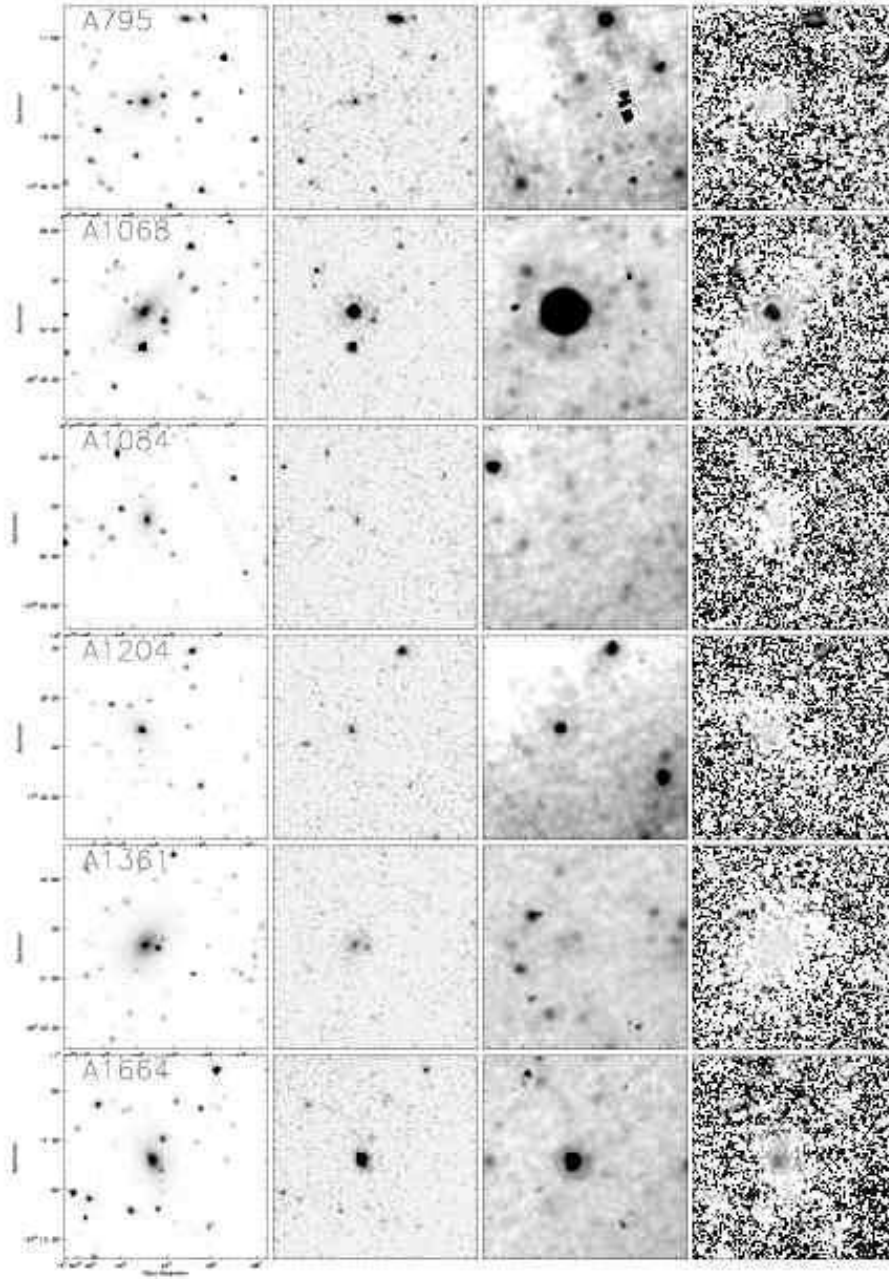


Fig. 2.— continued

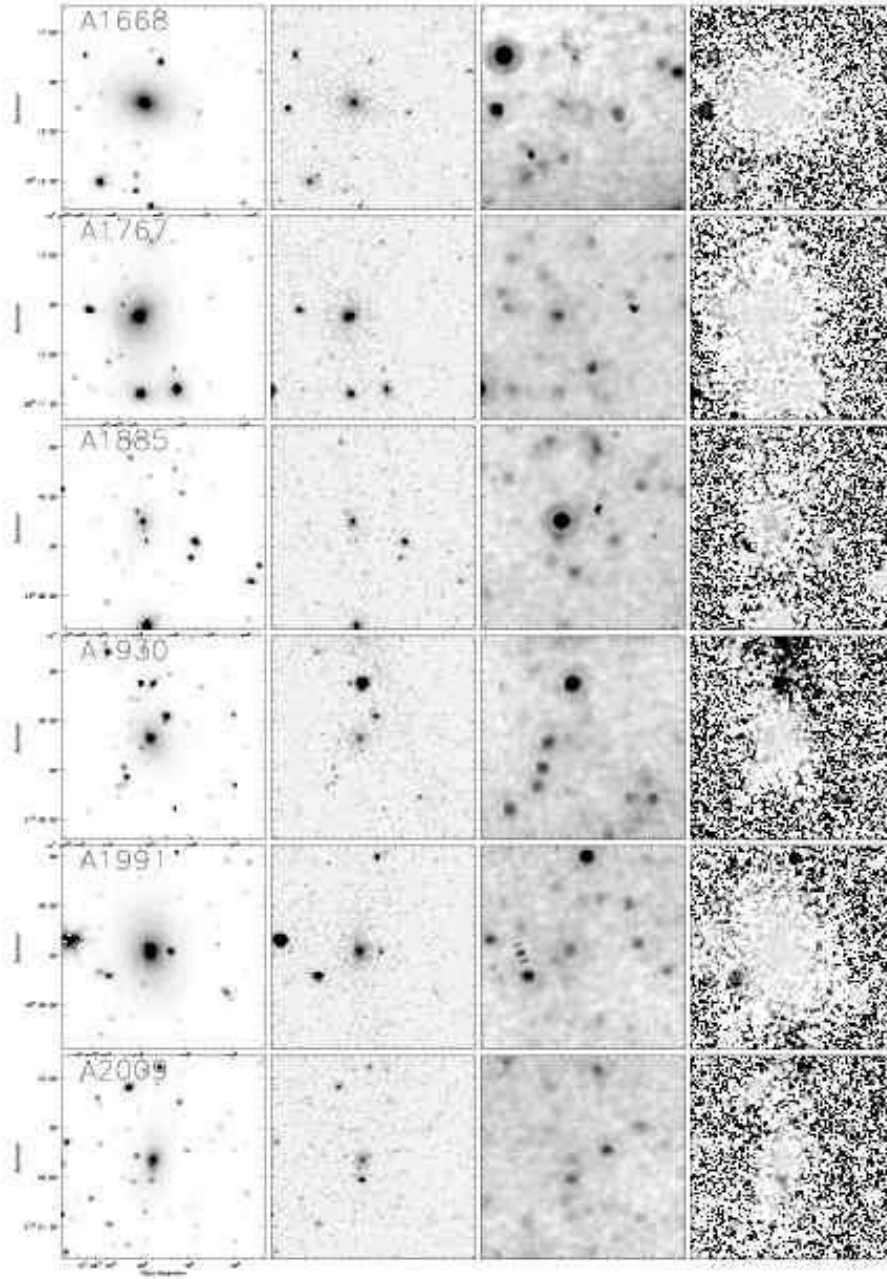


Fig. 2.— continued

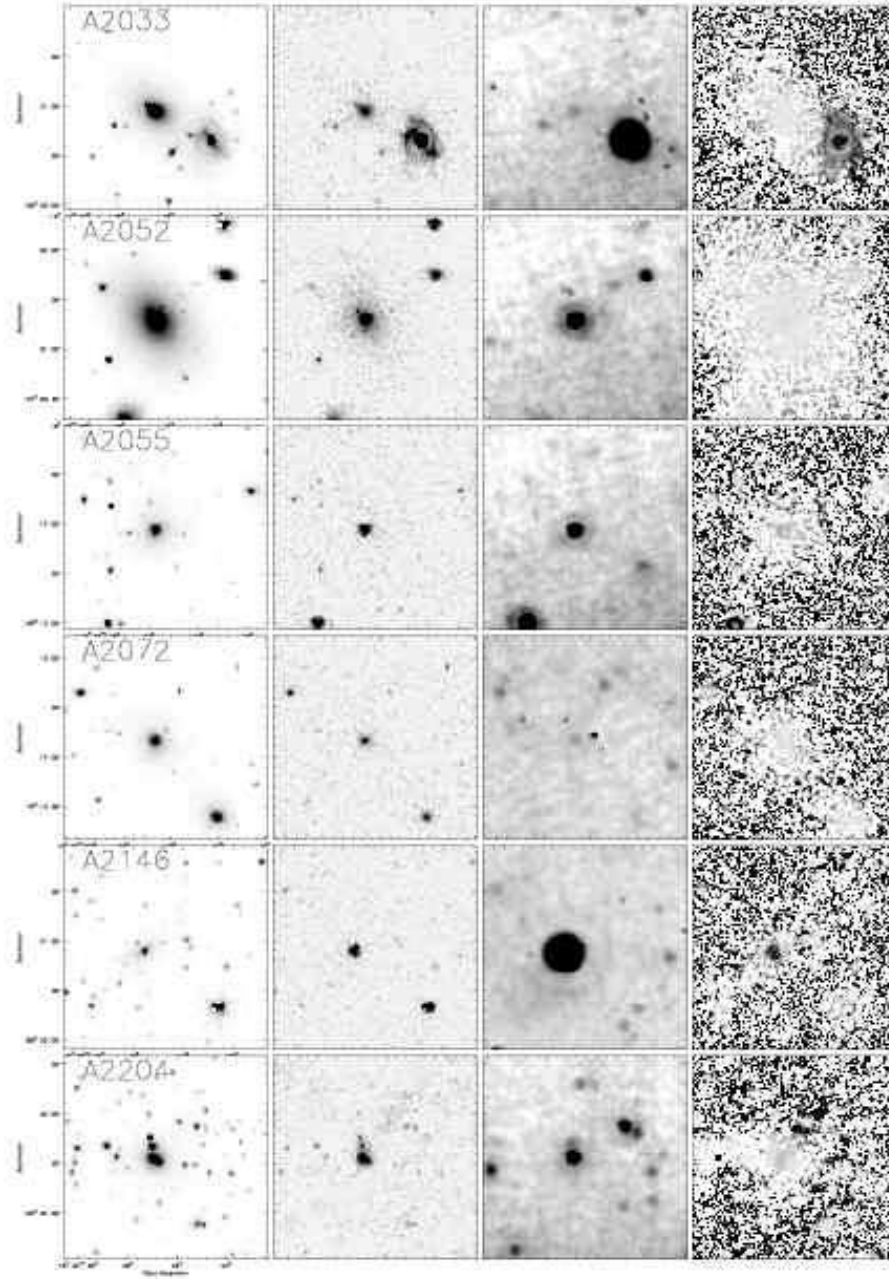


Fig. 2.— continued

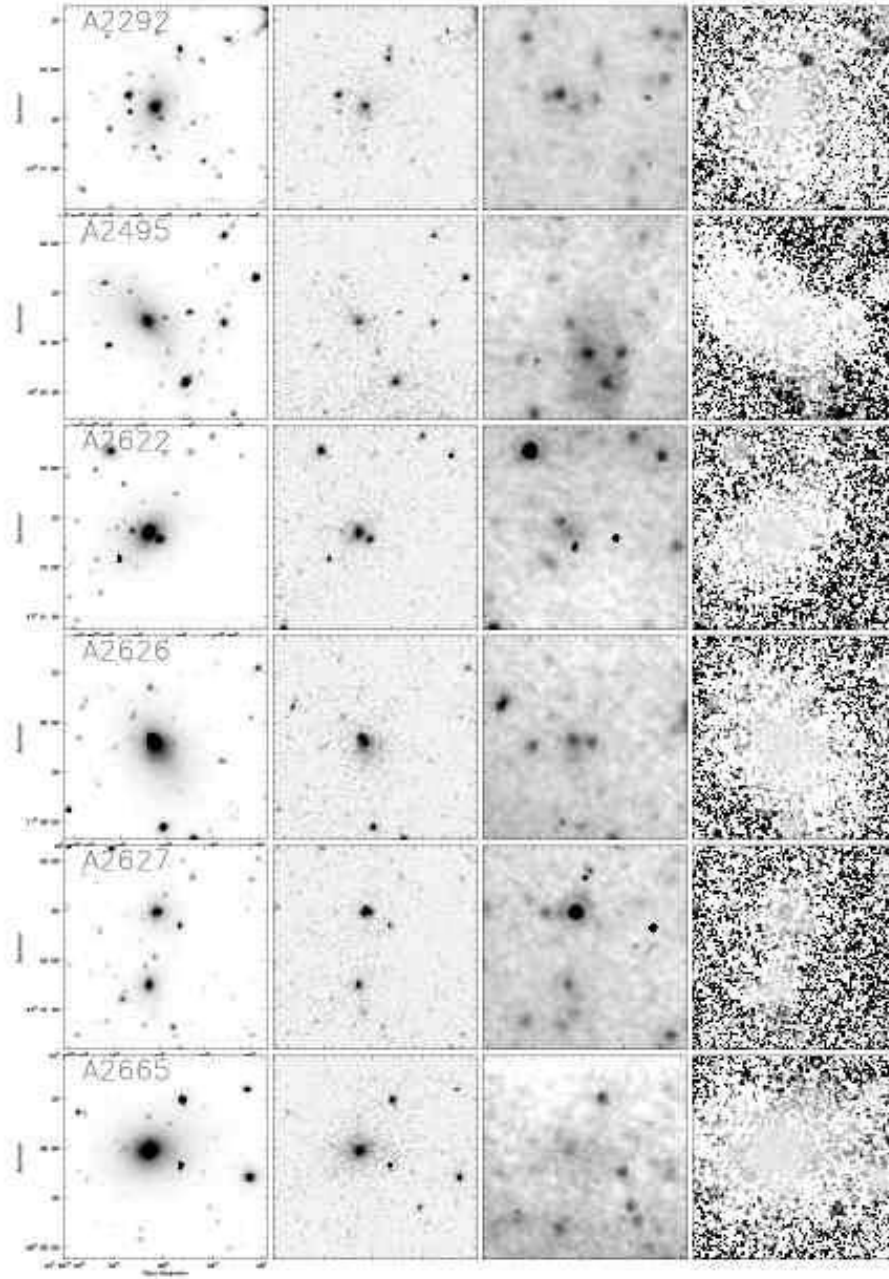


Fig. 2.— continued

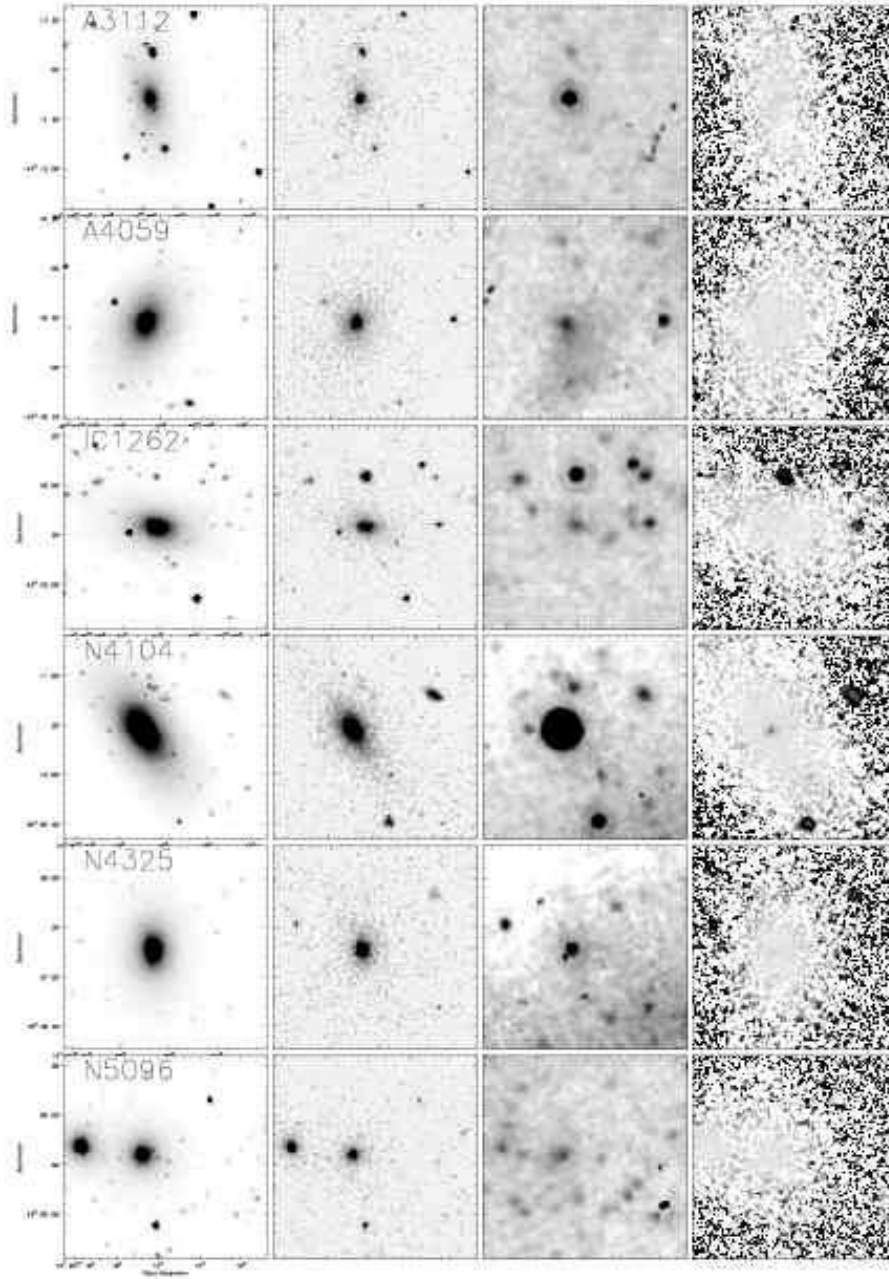


Fig. 2.— continued

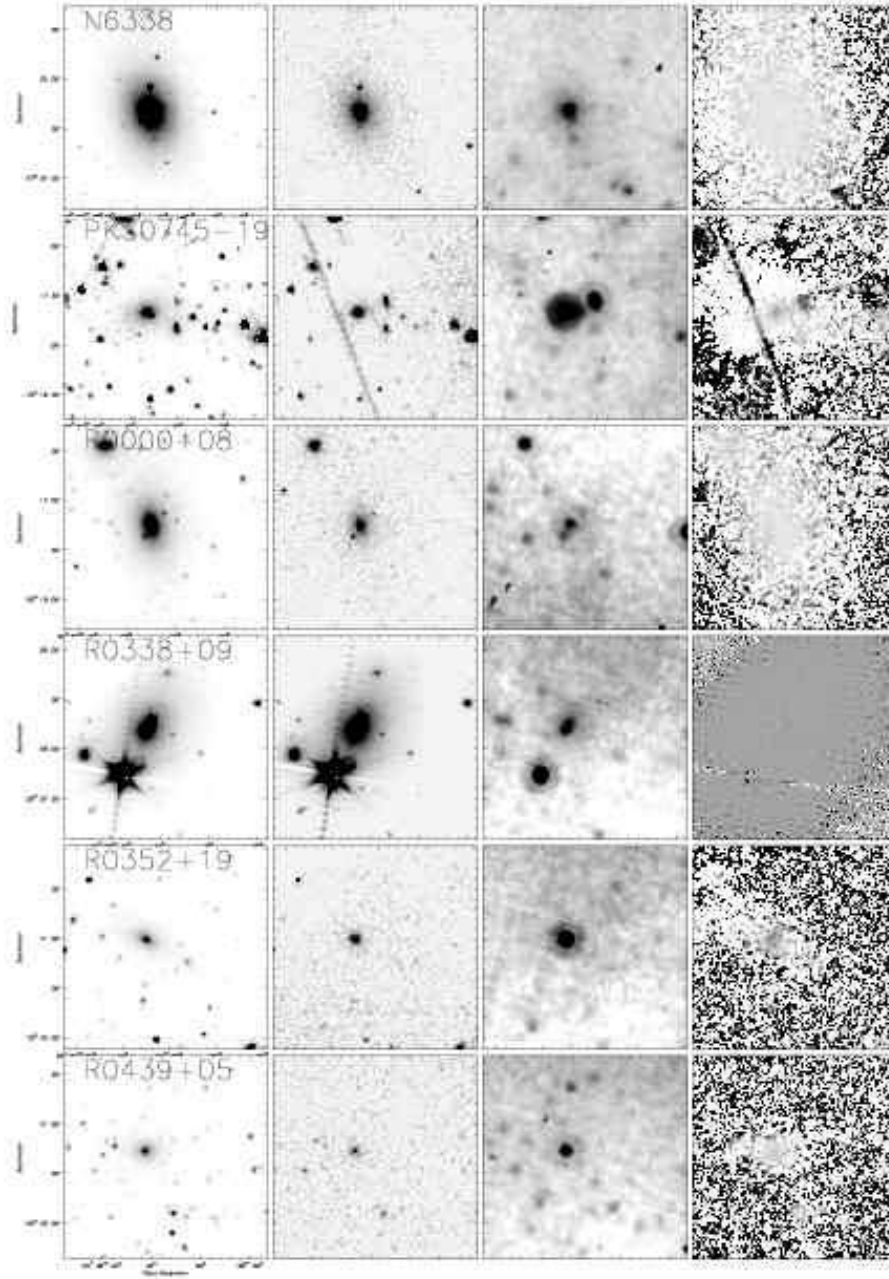


Fig. 2.— continued



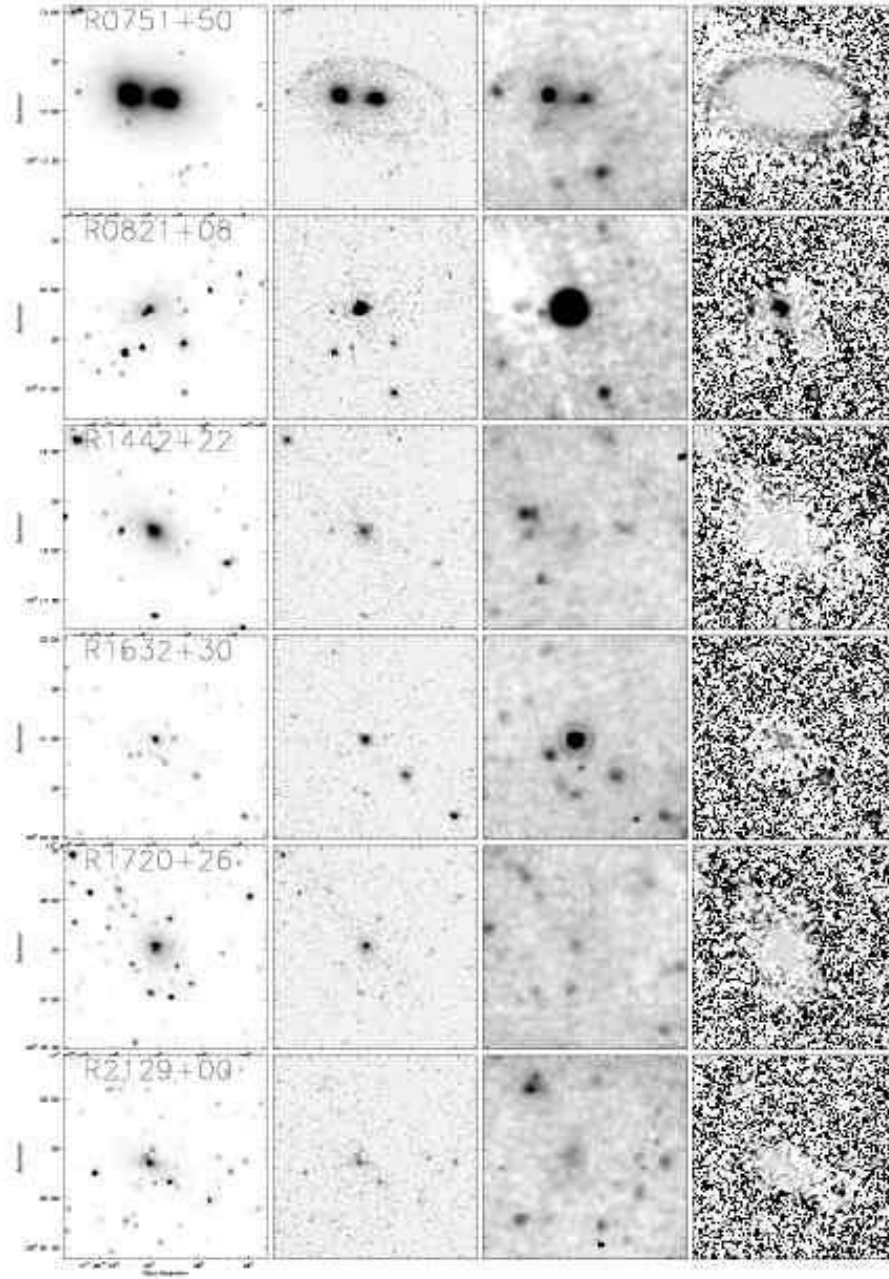


Fig. 2.— continued



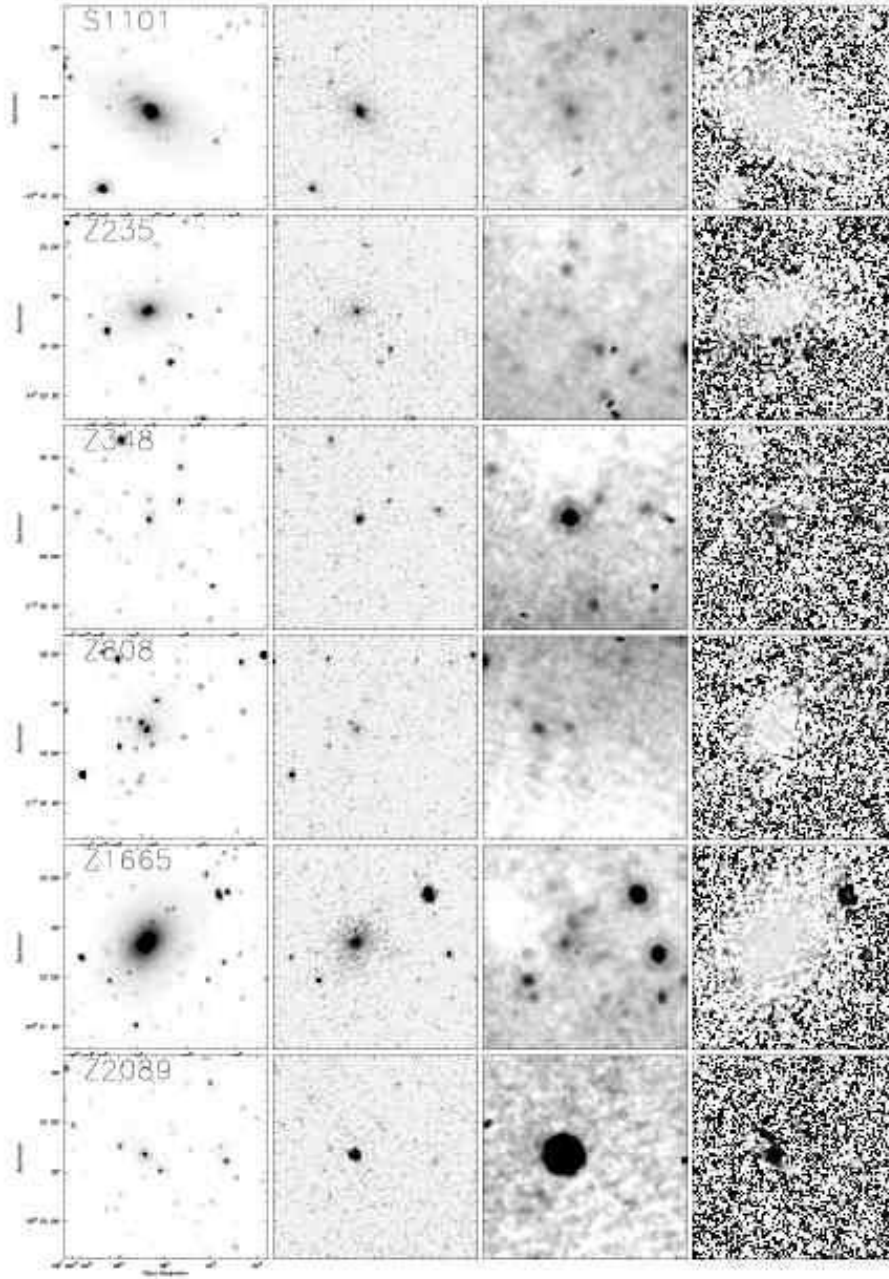


Fig. 2.— continued

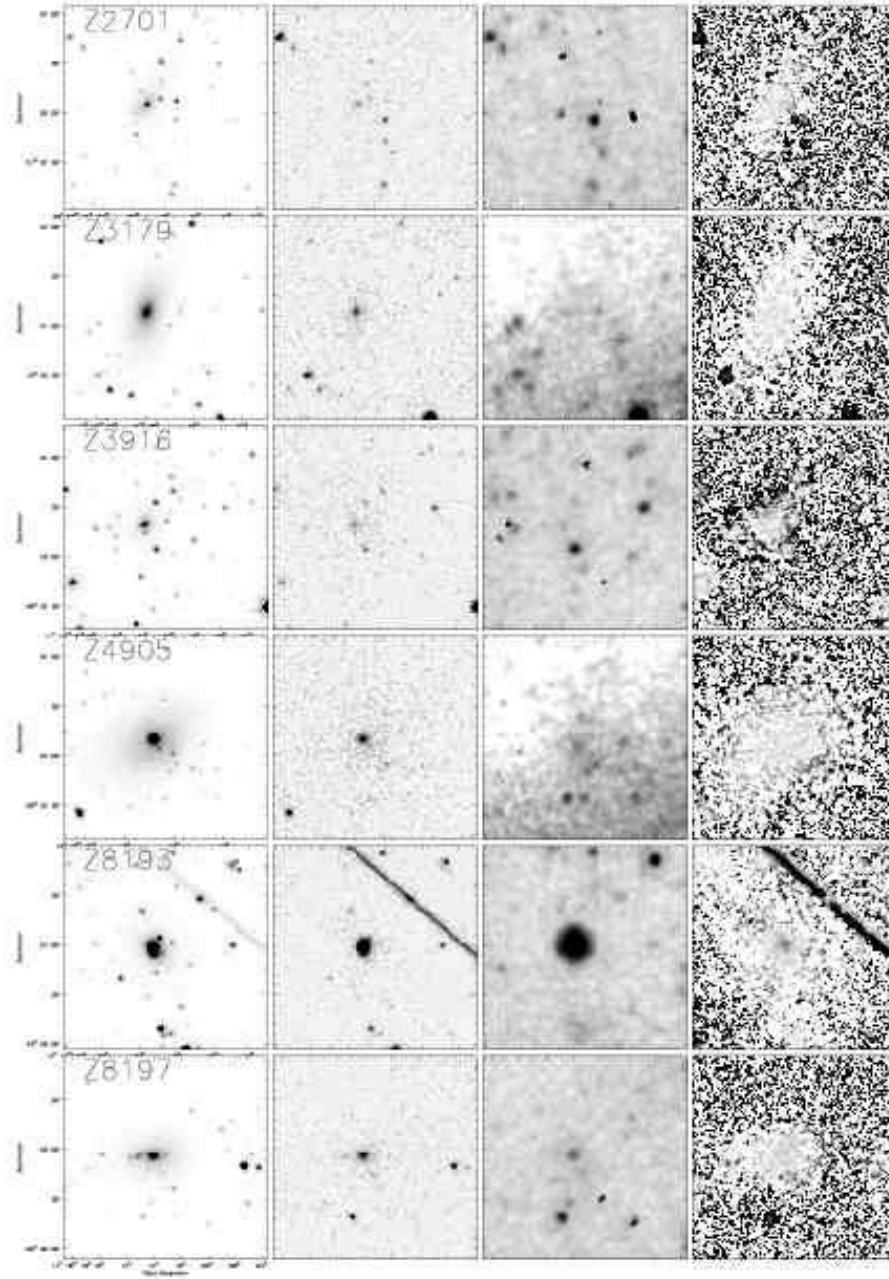


Fig. 2.— continued

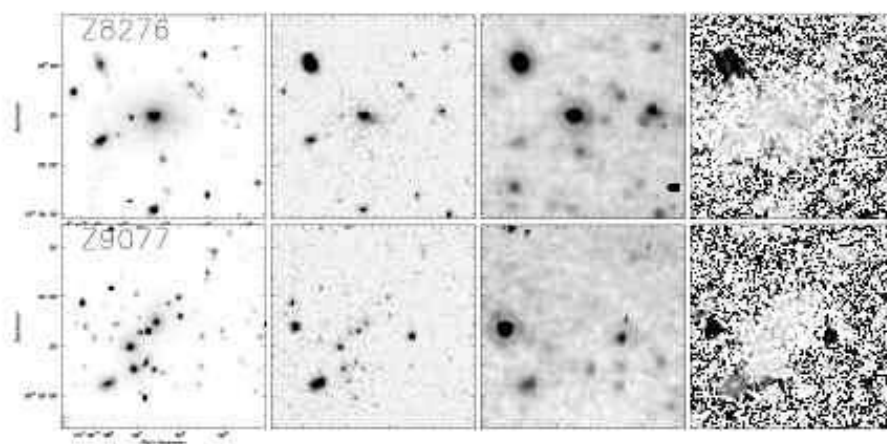


Fig. 2.— continued

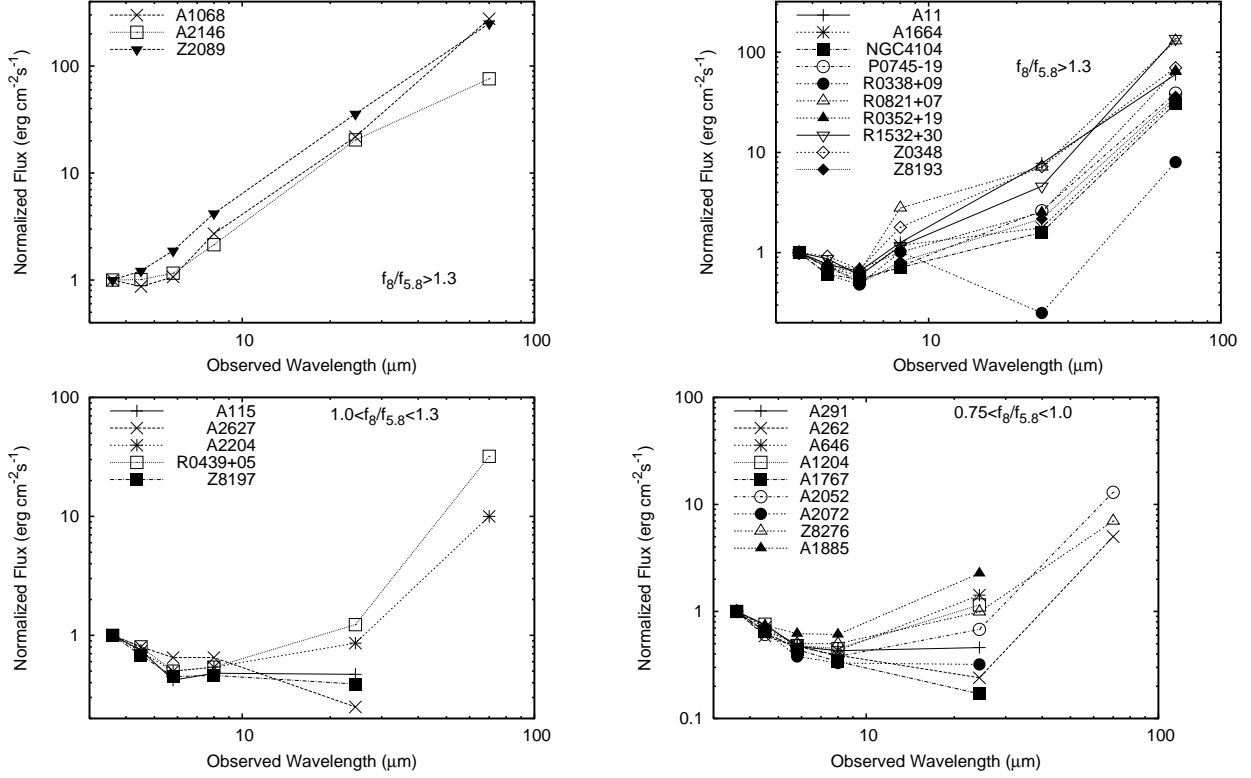


Fig. 3.— Spectral energy distributions of the brightest cluster galaxies. We have grouped them by  $5.5/8.0 \mu\text{m}$  color. The fluxes are normalized to the  $3.6 \mu\text{m}$  flux. a) These objects are among the reddest objects with  $F_{8\mu\text{m}}/F_{5.8\mu\text{m}} > 1.3$ . They also have unresolved red nuclei seen in the IRAC color maps. These three have high  $[\text{OIII}]/\text{H}\beta$  ratios suggesting that they host an AGN. Abell 2146 has a blue  $24$  to  $70 \mu\text{m}$  flux ratio suggesting that the dust is warmer than the others. b) Additional galaxies with  $F_{8\mu\text{m}}/F_{5.8\mu\text{m}} > 1.3$ . These galaxies have strong mid-infrared excesses compared to a quiescent elliptical galaxy and all were detected at  $70\mu\text{m}$ . c) BCGs with  $1.0 < F_{8\mu\text{m}}/F_{5.8\mu\text{m}} < 1.3$ . d,e) BCGs with  $0.75 < F_{8\mu\text{m}}/F_{5.8\mu\text{m}} < 1.0$ . f,g) BCGs with  $F_{8\mu\text{m}}/F_{5.8\mu\text{m}} < 0.75$ . Most of these are consistent with a quiescent stellar population. Objects that are not detected at  $70\mu$  have upper limits on this plot at  $70\mu\text{m} \sim 3\text{--}10$  times the flux at  $3.6\mu\text{m}$ . h) Additional BCGs with  $F_{8\mu\text{m}}/F_{5.8\mu\text{m}} < 0.75$  and that are detected at  $70\mu\text{m}$ .

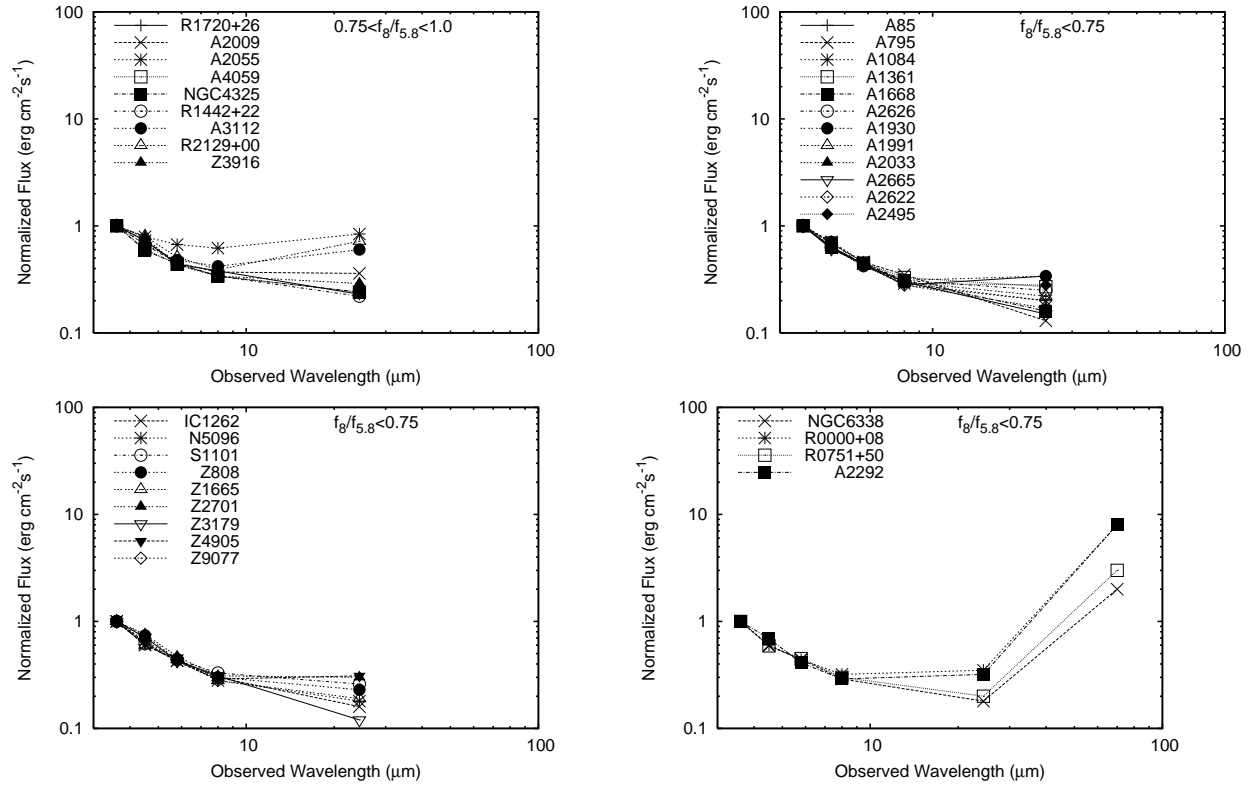


Fig. 3.— continued

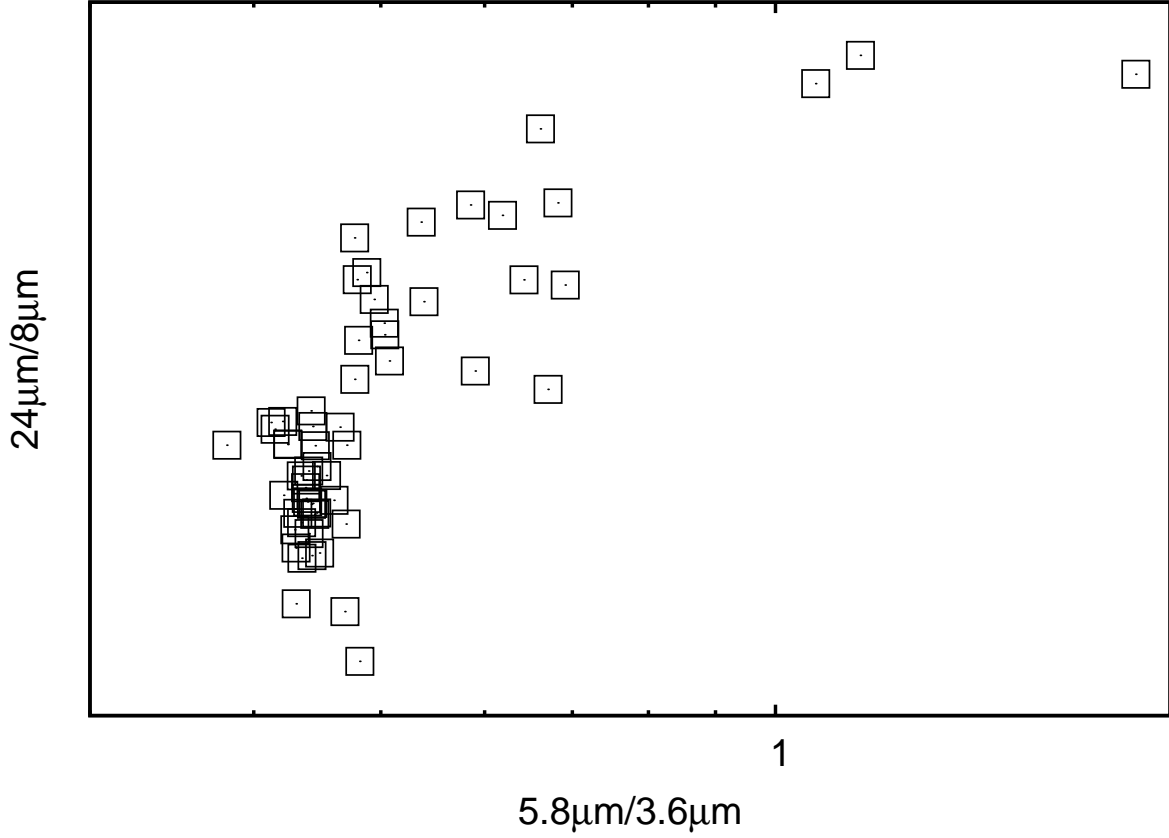


Fig. 4.— Infrared color-color plot. Each axis is the ratio of the fluxes at the listed wavelengths. Clusters with a  $5.8/3.6\ \mu\text{m}$  flux ratio less than 0.5 and a  $24/8\ \mu\text{m}$  flux ratio less than 2 are quiescent. The two color ratios are correlated but with larger scatter in the  $24/8\ \mu\text{m}$  ratio than at shorter wavelengths. Objects with flux ratios  $F_{5.8}/F_{3.6} \gtrsim 0.5$  or  $F_{24}/F_8 \gtrsim 1$  have infrared excesses. The three objects at the top right of the plot are Abell 1068, Abell 2146 and Z2089 with unresolved red nuclear sources in the IRAC bands indicating the presence of hot dust. These three also have high measured  $[\text{OIII}]/\text{H}\beta$  ratios and so probably host a dusty AGN.